Characterization of the metasomatizing agent in the upper mantle beneath the northern Pannonian Basin based on Raman imaging, FIB-SEM and LA-ICP-MS analyses of silicate melt inclusions in spinel peridotite

Nóra Liptai[1,2*], Márta Berkesi[1], Levente Patkó[1,3], Robert J. Bodnar[4], Suzanne Y. O'Reilly[2], William L. Griffin[2], Csaba Szabó[1,5]

[1]Lithosphere Fluid Research Lab, Institute of Geography and Earth Sciences, Eötvös University, 1/C Pázmány Péter sétány, Budapest, H-1117, Hungary

[2]Australian Research Council Centre of Excellence for Core to Crust Fluid Systems (CCFS) and GEMOC, Department of Earth and Planetary Sciences, Macquarie University, Herring Rd., North Ryde, NSW 2019, Australia

[3]Institute for Nuclear Research, Isotope Climatology and Environmental Research Centre, 18/C Bem tér, Debrecen, 4026, Hungary

[4]Fluids Research Laboratory, Department of Geosciences, Virginia Tech, 926 West Campus Drive, Blacksburg (VA), 24061, USA

[5]Geodetic and Geophysical Institute, Research Centre for Astronomy and Earth Sciences, 6-8 Csatkai Endre u., Sopron, 9400, Hungary

*Present address: MTA CSFK Lendület Pannon LitH_2Oscope Research Group, Geodetic and Geophysical Institute, Research Centre for Astronomy and Earth Sciences, 6-8 Csatkai Endre u, Sopron, 9400, Hungary

Abstract

Silicate melt inclusions (SMI) containing several daughter minerals, residual glass and a CO_2 bubble were analyzed to constrain the composition and evolution of the metasomatic melt present in the upper mantle beneath the Nógrád-Gömör Volcanic Field (NGVF), northern Hungary – southern Slovakia. The SMI were analyzed with a combination of Raman spectroscopy, FIB-SEM and LA-ICP-MS to identify phases and obtain their volume proportions and major- and trace-element geochemistry. Slicing through the entire volume of the inclusions and collecting geochemical information at each slice with FIB-SEM allowed us to model the 3D appearance of the phases within the SMI, and to use this information to calculate bulk major-element compositions.

The partially crystallized SMI are hosted in clinopyroxene in a lherzolite xenolith that shows evidence of a metasomatic event that altered the lherzolites to produce wehrlites. Based on bulk compositions, the SMI trapped the metasomatic melt linked to wehrlite formation in the NGVF. The melt is enriched in Fe and has an OIB-like trace-element pattern, which suggests an intraplate mafic melt similar to the host basalt, but with slightly different chemistry. Pre-entrapment evolution and reaction with the lherzolite wall rock produced an intermediate melt composition. Petrogenetic modeling indicates that the melt was generated as a result of a very small degree of partial melting of a garnet lherzolite source. Following entrapment, a volatile bubble exsolved from the residual melt during ascent to shallow depths as suggested by consistent densities of CO_2 in vapor bubbles. Small crystals, including sulfates and mica, that formed at the boundary of the bubble and the glass indicate that the exsolved fluid originally contained S and H_2O, in addition to CO_2.

Introduction

Primary silicate melt inclusions (SMI) hosted by upper mantle minerals have been commonly used to characterize the melts that infiltrate and react with the mantle phases (e.g., Schiano et al. 1992; 2000; Szabó et al. 1996; 2009; Zajacz et al. 2007; Hidas et al. 2010; Duan et al. 2014). The SMI are considered to represent the original melt composition at the time of entrapment at mantle conditions (Schiano et al. 1992; 2000; Frezzotti 2001). The trapped melt droplet remains isolated, i.e., behaves as a closed system and evolves independently from the host (e.g., Roedder 1984) because of the high elastic modulus of the host minerals that prevents decompression and volumetric changes during and after ascent to the surface (Schiano and Bourdon 1999). However, diffusion into or out of the SMI may still occur to different extents for different elements, depending on the concentrations and diffusion coefficients of the given element in the host mineral. Therefore, in general, the elements most likely to retain their original concentrations in the SMI are those that are least compatible with the host (Qin et al. 1992). Consequently, melt inclusions, if present in great abundance, can be a significant reservoir for incompatible trace elements and volatiles that tend to partition in the melt.

Fluid and silicate melt inclusions are common in peridotite xenoliths of the Carpathian-Pannonian region (CPR) and have been the subject of numerous studies, especially from the Bakony-Balaton Highland (e.g., Török 1995; Szabó et al. 2009; Hidas et al. 2010; Berkesi et al. 2012). The melt inclusions have been interpreted to represent a mafic melt of asthenospheric origin, which obtained an evolved character via interaction with a metasomatized mantle prior to entrapment (Szabó et al. 2009). In the Nógrád-Gömör Volcanic Field (NGVF), two types of SMI have been described. Olivine-hosted SMI in xenoliths from one locality were interpreted to be remnants of a volatile-rich, subduction-related melt which was also responsible for modal metasomatism in the xenoliths (Szabó et al. (1996). These SMI had variable compositions (basaltic to andesitic), which was explained by

entrapment at different stages of melt evolution. The other type of SMI hosted in olivine in clinopyroxene-rich cumulate xenoliths represents an evolved version of the alkali basaltic melt underplating the Moho prior to eruption of the host magma (Zajacz et al. (2007).

Previous studies (Liptai et al. 2017; Patkó et al. 2020) classified peridotite xenoliths in the NGVF into two suites based on their modal composition and texture: a dominant 'lherzolitic' suite with no or minimal textural evidence for metasomatism and with both ortho- and clinopyroxenes present as individual grains , and a 'wehrlitic' suite, with clear reaction textures and orthopyroxene absent, except for minor remnant cores within clinopyroxene and olivine. It has been established that the wehrlite suite is the product of interaction between an infiltrating mafic melt and the lherzolite wall rock (Patkó et al. 2020). Recently, primary SMI have been found in clinopyroxene in a xenolith that is part of the lherzolite suite, based on the presence of orthopyroxene. The goal of this study is to characterize the origin, trapping conditions and post-entrapment evolution of these SMI.

Geological setting

The Pannonian Basin in the Carpathian-Pannonian region (CPR) formed during the late Oligocene – early Miocene following the juxtaposition of two microterranes, the Alcapa and Tisza-Dacia (Csontos et al. 1992). During the Neogene, extension driven by subduction rollback on the eastern margin of the CPR (Horváth 1993; Csontos 1995) dominated the tectonics of the region. The extension was accompanied by asthenospheric uplift and resulted in extreme thinning of the lithosphere (Horváth 1993). Following the termination of extension in the late Miocene (~8–7.5 Ma), a large-scale tectonic inversion was initiated by the ongoing push and rotation of the Adria block against the European platform, resulting in a change

from extensional to compressional kinematics (Horváth and Cloetingh 1996; Bada et al. 2007).

Beginning in the late Miocene, but mostly during Plio-Pleistocene time, a series of alkali basalt eruptions occurred throughout the CPR, generated via decompressional melting associated with asthenospheric upwelling (Embey-Isztin et al. 1993). The alkali basalts are known to have sampled the upper mantle in at least five locations in the CPR, from west to east: Styrian Basin, Little Hungarian Plain, Bakony-Balaton Highland, Nógrád-Gömör and Perşani Mountains (Fig. 1a).

Based on detailed petrographic observations and geochemical analyses of upper mantle xenoliths, Liptai et al. (2017) defined three major mantle domains beneath the Nógrád-Gömör Volcanic Field (NGVF) (see their Figure 1) referred to as the northern, central, and southern areas. K–Ar ages of the xenolith-hosting basalts are 6.4–4.9 Ma in the northern area, 4.0–2.5 Ma in the central area and ~2.5 Ma in the southern area (Balogh et al. 1981; 1986 and unpublished data). Similar ages were obtained by U/Pb and (U–Th)/He dating for the northern and central areas (7.0 - 5.9 and 3.0 - 1.7 Ma, respectively; Hurai et al. 2013). Smaller lava flows and maars are characteristic of the xenolith-hosting alkali basalts in the northern and southern areas, whereas the central area is dominated by two large lava flows (Babi Hill and Medves Plateau) (e.g., Konecný et al. 1995) (Fig. 1b). The sampling location of the xenolith studied in this paper, Fil'akovo-Kerčik, is interpreted to represent an eroded lava flow (Lexa et al. 2010) and previous studies of xenoliths from this location confirm its association with the upper mantle beneath the Babi Hill and the Medves Plateau (Liptai et al., 2017).

Sample petrography and mineral chemistry

Xenolith NFL1327 containing the SMI studied here is assigned to the 'lherzolitic' suite of the NGVF (Liptai et al. 2017) based on the presence of orthopyroxene as individual grains. The petrography and geochemistry of the xenolith are described by Liptai et al. (2017), and the results are summarized here and in Supplementary Table 1. The xenolith is modally a wehrlite containing 88 vol% olivine, 10 vol% clinopyroxene, 1 vol% orthopyroxene and 1 vol% spinel. The texture of the xenolith is equigranular, and clinopyroxenes appear in clusters (Fig. 2a), whereas olivine-rich areas show the characteristic texture of the wehrlite suite (Patkó et al. 2020). The sample bears microstructural evidence of deformation and subsequent annealing, interpreted to be the result of metasomatizing melts percolating through the sample prior to ascent to the surface (Liptai et al. 2019).

Olivine, orthopyroxene and clinopyroxene have relatively low Mg-numbers (100*Mg/[Mg+Fe] = 85, 88 and 87, respectively) compared to the majority of the lherzolite suite (90–91), which reflects an enrichment in Fe. In addition to Fe, Mn shows high concentrations in olivine (0.25 oxide wt. %) and orthopyroxene (0.25 oxide wt. %) as well, and spinel has an elevated Ti-content (0.41 oxide wt%). Trace element contents of pyroxenes show enrichment in light rare earth elements (LREE) and depletion in Rb, Ba, and Pb. Based on these geochemical characteristics, the xenolith was classified as 'Group IIB' by Liptai et al. (2017). This group represents a transitional type between the lherzolite and a wehrlite suite as the enrichment in Fe, Mn, Ti, and LREE are characteristic of the wehrlites (Patkó et al. 2020), but the textures and the abundance of modal orthopyroxene are more similar to the lherzolite suite. The studied xenolith contains several clinopyroxene grains with primary SMI randomly distributed within each grain (Fig. 2b).

Analytical techniques

147 *Raman spectroscopy*

148

149 Raman spectroscopy is an ideal tool to interrogate the composition of SMI because it
150 is non-destructive and offers spatial resolution on the order of 1 micron as well as detailed
151 mapping (Bodnar and Frezzotti 2020). Raman analyses included point analyses of constituent
152 phases in the SMI and imaging of three complete silicate melt inclusions (SMI_2, SMI_R,
153 SMI_U). Analyses were conducted at the Research and Instrument Core Facility of the
154 Faculty of Science at Eötvös University, Budapest. The instrument used was a confocal
155 HORIBA Labram HR spectrometer with a Nd:YAG 532 nm wavelength laser excitation and
156 600 or 1800 grooves/mm optical grating, 50-100 μm confocal hole, 5–80 s acquisition time
157 and a 100x long working distance objective. Laser power was 130 mW at the source and ~50
158 mW at the sample. Using a 50 μm confocal hole and 1800 grooves/mm grating, the laser spot
159 diameter was measured to be ~1.4 μm and the depth resolution was ~1.7 μm. The spectral
160 resolution using the 1800 grooves/mm optical grating was 0.7 cm^{-1} at 1398.5 cm^{-1} and 0.6 cm^{-1}
161 at 2331 cm^{-1} (defined as the measured full width at half maximum values of two neon
162 atomic emission lines). We note that after peak fitting, a peak position can generally be
163 determined to within ±0.03 cm^{-1} (Lin et al. 2007). Both imaging and analyses of individual
164 phases (where needed) were carried out in the spectral range from 220 to 1900 cm^{-1} initially,
165 and then from 2750 to 4000 cm^{-1} to test for the presence of OH-bonds in hydrous phases.
166 Image mapping at room temperature was conducted using the 600 grooves/mm optical
167 grating, with a step size of 0.5–0.7 μm. Acquired spectra were processed using LabSpec v5.
168 software. For phase identification, the databases of Frezzotti et al. (2012) and the online
169 database of rruff.info (Lafuente et al. 2015) were used.

170

171 *FIB-SEM*

172

173 The FIB-SEM technique was applied to four selected silicate melt inclusions (SMI_2,
174 SMI_3, SMI_R and SMI_U), three of which had previously been imaged with Raman
175 spectroscopy. The analyses were conducted in the Research and Instrument Core Facility at
176 Eötvös University, Budapest, with the use of an FEI Quanta 3D dual-beam scanning electron
177 microscope with both secondary- and backscattered-electron detectors. The instrument is also
178 equipped with a silicon drift X-ray energy dispersive (SDD-EDX) detector, which has
179 recently been shown to provide about the same level of precision and accuracy as wavelength
180 dispersive spectrometers (e.g., Ritchie et al. 2012). The accelerating voltage was 10–20 keV,
181 depending on the size of the inclusion and the elements of interest. The beam current was
182 0.02–4 nA, which permitted the detection of major elements from carbon to barium.
183 The application of the FIB-SEM technique to fluid inclusions was described in detail by
184 Berkesi et al. (2012), and is summarized in the following steps: (1) a thin (200–300 nm)
185 platinum layer is deposited on the carbon-coated sample surface to mark the location of the
186 inclusion; (2) the sample is then tilted by 52°, so that the milling ion beam is perpendicular to
187 the surface and the electron beam is at a 38° angle; (3) an additional platinum layer of ~1–2
188 μm is deposited on the pre-selected area as protection from abrasion by the Ga-ion beam
189 (Wirth 2004); (4) trenches are excavated on three sides of the platinum strip using a higher
190 beam current (15–45 nA) to accommodate the waste material produced by the milling (Fig.
191 3a), (5) slices of equal thickness (400 nm) are milled through the SMI for easier volume
192 reconstruction, exposed phases are analyzed with SEM-EDX, and electron images for each
193 slice are saved (Fig. 3b). Identification of the daughter phases was based on previously
194 obtained Raman spectra, morphology shown on the secondary electron images, brightness on
195 the backscattered electron images, and/or major-element contents inferred from the SEM-
196 EDX spectra. Due to the small size of the daughter minerals (~1–10 μm), the SEM-EDX

spectra generally contained mixed signals from the analyzed phase and the adjacent area (host and/or other daughter phases). A spectrum of the host was collected at every slice where daughter phases of the SMI were analyzed, for comparison and better discrimination of the signals. Volume proportions of the constituent phases were determined with Amira™ software developed by Thermo Scientific; the method involves defining the daughter phases on each slice, and then extrapolating the areas to acquire phase volumes between the slices, producing a 3D reconstruction of the entire SMI (Fig. 3c).

LA-ICP-MS

Trace-element concentrations of bulk silicate melt inclusions were determined at the Department of Geosciences, Virginia Tech (Blacksburg, VA, USA), with the use of an Agilent 7500ce quadrupole ICP-MS coupled with an ArF Excimer Laser system. The laser acquisition parameters were: 193 nm wavelength, ~7–10 J/cm^2 energy density, 5 Hz repetition rate and 24–32 μm spot size. The ~ 1.5 cm^3 ablation cell was flushed with He gas at ~ 1.2 L/min; auxiliary Ar gas flow was 1.03 L/min. For each isotope, a 10 ms dwell time was applied. For the external standard, the NIST-612 synthetic glass was used; average Ca concentration, previously obtained by mass-balance calculation for bulk SMI from SEM-EDX analyses, was used for the internal standard. This approach is valid owing to the overall low variability in major-element compositions in the SMI analyzed with FIB-SEM, and we assume that all primary SMI have similar geochemical compositions. Data reduction was carried out using the AMS software of Mutchler et al. (2008). Owing to the small size of the SMI, the laser spot was somewhat larger than the size of the SMI, producing a signal that had a mixed character (host + SMI). To separate the contribution of the host from the signal from the SMI, we followed the calculation procedure described by Halter et al. (2002), as

implemented in the software of Mutchler et al. (2008). This calculation uses the concentration of an element that is known for both the inclusion and the host clinopyroxene as an internal standard. The estimation of uncertainty was carried out based on the study of Longerich et al. (1996).

Silicate melt inclusion petrography

The silicate melt inclusions (SMI) usually have isometric or slightly elongated shapes and range from 5 to 20 μm in longest dimension (Fig. 2). They are partially crystallized, and a vapor bubble, glass and several crystals are observable in polarized light (Fig. 4); the crystals are collectively referred to as daughter phases, and are assumed to have crystallized from the trapped melt during cooling (e.g., Frezzotti 2001). Crystal sizes range from a few μm up to 10 μm, whereas the size of the bubble is proportional to the size of the whole inclusion. Two-dimensional Raman imaging in the plane of maximum dimension of the inclusions allowed identification of daughter phases in three selected SMI (SMI_2, SMI_R, SMI_U; Fig. 4). All three SMI contain apatite (Raman bands at 428, 578, 960 and 1070 cm^{-1}) and a volatile-bearing mineral (either amphibole or mica; Raman band at 3675 cm^{-1}). In addition, sulfates including anhydrite (Raman bands at 497, 607, 625, 1109, 1127 and 1159 cm^{-1}) and barite (Raman bands at 460, 627 and 993 cm^{-1}) were found in SMI_2, and clinopyroxene on the SMI wall (hereafter referred to as 'wall clinopyroxene'), with a spectrum that is slightly different from that of the clinopyroxene host (extra band at 535 cm^{-1}), was identified in SMI_R. Characteristic Raman spectra of the sulfates, the vapor bubble and the wall clinopyroxene are shown in Fig. 4, along with the reference spectrum of the host clinopyroxene. The vapor bubble in all three analyzed SMI contains CO_2, based on the presence of the Fermi diad

(Fermi 1931). The bands of the Fermi diad appear at 1283.5–1387.0, 1284.7–1388.3, and 1284.7–1388.3 cm^{-1} in SMI_2, SMI_R and SMI_U, respectively (Table 1).

FIB-slicing and subsequent SEM-EDX analyses of the melt inclusions confirmed the identification of daughter minerals based on Raman spectroscopy, and revealed additional daughter phases, (sometimes two or more distinct grains of the same phase, as described below) which were too small (i.e., sub-micrometer size) to detect with the petrographic microscope or by Raman spectroscopy. The largest volatile-bearing mineral (up to ~10 μm) in all four analyzed SMI was identified as amphibole based on the SEM-EDX spectra; in SMI_3, two distinct amphibole grains are present. Mica appears in all four SMI as well, and always occurs adjacent to the gas bubble (Fig. 3b). SMI_U contains two distinct ~6–8 μm mica flakes (see BSE images on Fig. 3b). Spinel and apatite are present in all four SMI, the former appearing as an isometric crystal on the border between the glass and clinopyroxene, and the latter is present either as several small (< 1 μm) grains (SMI_U, Fig. 3b) or has an elongated needle shape (e.g., SMI_R; Fig. 5). Sulfide blebs were detected in SMI_R and SMI_U, and tiny (< 1 μm) sulfates (anhydrite ± barite) were observed in SMI_R (Fig. 5), SMI_2 and SMI_3. Note that in SMI_R, both sulfide and sulfate daughter phases are present. The recognition of clinopyroxene that precipitated from the melt onto the inclusion wall was made difficult due to the similarity in composition to the host clinopyroxene; however, irregularities in the shape of the inclusion (e.g., Fig. 5) and SEM spectra yielding slightly different compositions could be used. It is still likely that the modal proportions of clinopyroxene is underestimated and should be considered as a minimum.

Volume proportions acquired with the Amira™ software are shown in Table 2. The modal compositions of the SMI are quite similar to one another. Approximately half of the inclusion volume (43–53 vol. %) is glass. Amphibole and mica show a slightly wider modal range, being present at 22–32 and 0.2–1.2 vol. %, except for SMI_U, where mica is more

abundant (9.4 vol. %) than amphibole (7.5 vol. %). Wall clinopyroxene comprises 7–19 vol. % of the inclusions. Spinel, apatite, sulfide, anhydrite and barite (where present) each are usually below 2 vol. %.

Silicate melt inclusion geochemistry

Major element composition

Major-element compositions were acquired from SEM-EDX spectra for the most abundant daughter phases (Table 3, Fig. 5). In the case of volatile-bearing phases, compositions were corrected to sum to a total less than 100 % to account for the volatile content, i.e., 97.5, 96.5 and 95.5 wt. % for amphibole, mica and glass, respectively; taken from average values of daughter minerals of SMI in (Szabó et al. 1996) and from the glass phase in SMI of wehrlite xenoliths from the central NGVF (Patkó et al. 2018). Spinel compositions were corrected by omitting oxides (SiO_2, CaO, Na_2O, K_2O) expected to be present only in surrounding silicate phases and glass. The resulting compositions of the four melt inclusions are similar, as described below.

Clinopyroxene precipitation on the inclusion wall (i.e., wall clinopyroxene) was generally difficult to distinguish from the host, however, several analyses in SMI_2 and SMI_R revealed slightly different major-element compositions. This difference is observable as an increase in FeO (8.5–9.5 wt. %) and Al_2O_3 (5.6–6.1 wt. %) at the expense of MgO (10.4–11.3 wt. %), whereas FeO and Al_2O_3 are lower in the host clinopyroxene, and MgO is higher (5.8–6.4, 4.1–4.9 and 11.9–14.2 wt. %, respectively; Table 3). Amphibole shows little compositional variability among the different SMI and are strikingly enriched in FeO (12.3–14.8 wt. %) and TiO_2 (3.48–6.95 wt. %) compared to amphiboles in most lherzolites of the

296 NGVF suite (Liptai et al. 2017). In contrast, amphiboles have slightly lower SiO_2, Al_2O_3,
297 MgO and Na_2O contents. Mica grains are usually small, therefore the composition has a larger
298 uncertainty and shows wider variation. However, the enrichment in FeO and the depletion of
299 MgO is very strong, compared to mica (phlogopite) in the melt inclusions from NGVF
300 xenoliths described by Szabó et al. (1996). Spinel is dominantly iron-rich, with a small
301 proportion of chromium and aluminum. In SMI_U, the spinel is richer in aluminum and more
302 depleted in iron (Table 3). Glass is not entirely homogeneous; even on the BSE images of
303 several slices, numerous dark spots, possibly sub-micrometer sized bubbles, are observed.
304 Although the analyses did not identify the nature of these inhomogeneities, they revealed
305 some variability in the Na/K ratio of the glass. In most analyses, the glass appears to be K-rich
306 (K_2O = 2.9–6.0 wt. %), but several areas in SMI_2, SMI_R and SMI_U show Na_2O contents
307 up to 7.2–15.9 wt. % (Table 3). These Na-rich areas also have lower SiO_2-contents (52.0–59.6
308 wt. %). Similar compositional variability was reported by Szabó et al. (1996) in glass in melt
309 inclusions from the southern part of the NGVF. Furthermore, in SMI_U, the glass also has a
310 slightly elevated iron content (FeO = 2.3–3.4 wt. %).

311 Bulk major element compositions of the SMI were calculated by mass balance using the
312 compositions of individual phases comprising more than 0.5 vol. % of the inclusion (glass,
313 clinopyroxene, amphibole, ± mica, spinel, apatite; Table 2). The resulting compositions vary
314 within a narrow range among the four SMI. Concentrations of SiO_2 vary between 51.7 and
315 53.2 wt. %, and FeO contents are between 6.6–8.4 wt. %, which is significantly higher than
316 compositions reported by Szabó et al. (1996) from NGVF inclusions, and closer to the values
317 reported by Zajacz et al. (2007) for melt inclusions trapped in mafic cumulate xenoliths in the
318 NGVF. Apart from the high FeO content, the SMI compositions are in good agreement with
319 those found in wehrlite xenoliths from the NGVF (Patkó et al., 2018).
320

Trace element composition

Trace element contents of 8 additional SMI in clinopyroxenes from the studied xenolith were acquired by LA-ICP-MS analysis (Table 4). Only the analyses with mass factor (SMI ratio in the mixed ablation signal) ≥ 0.3 were considered. The compositions are similar for all 8 inclusions. Some of the heavy REE (Eu, Tb, Ho, Tm, Lu) yielded high uncertainties due to low concentrations and were therefore omitted from further interpretation. Nevertheless, the SMI produce similar patterns when normalized to primitive mantle composition (McDonough and Sun 1995) (Fig. 6). The SMI are enriched in incompatible elements such as Ba, Nb and Ta (117–530, 19.6–86.7 and 0.92–4.56 ppm, respectively); the concentrations are significantly higher than those in the host clinopyroxene of the xenolith (Supplementary Table 1). Hf and, to a lesser extent, Zr are also depleted. There is a continuous depletion from the light towards the heavy REE, with the former showing concentrations about one order of magnitude higher than the host clinopyroxene (Fig. 6). The most compatible elements (V, Cr, Ni) show the greatest depletion, similar to the pattern of the host clinopyroxene (Liptai et al. 2017).

Discussion

Composition of the metasomatic melt and pre-entrapment evolution

A significant advantage of the FIB-SEM technique compared to homogenization and bulk inclusion analysis is that it can provide high-resolution (sub-micrometer) 3D structural information on the daughter minerals within the inclusion, allowing us to draw conclusions on specific post-entrapment processes. This approach is similar to the recently published method

346 involving X-ray microtomography (Créon et al. 2018) and its high-resolution version
347 (Richard et al. 2018), which is capable of modelling the daughter phases of SMI in 3D.
348 However, a separate analytical procedure needs to be carried out to obtain chemical
349 compositions. With the use of the FIB-SEM-EDX system imaging, structural modelling and
350 major element chemistry can be acquired in one set of measurements, even if the latter may
351 have lower precision than electron microprobe analyses.

352 As was previously established (Liptai et al. 2017), multiple metasomatic events have
353 affected the upper mantle of the NGVF, and the last event resulted in Fe-, Mn-, Ti- and
354 LREE-enrichment in the minerals ('Group IIB'). It is suggested that this event can be linked
355 to the formation of the wehrlite series, which has similar geochemical characteristics (Liptai
356 et al. 2017; Patkó et al. 2020). Since that process involved an increase in the proportion of
357 clinopyroxene (Patkó et al. 2020), which also is the host mineral of the SMI in the studied
358 xenolith, the inclusions can be considered to represent the melt that interacted with the
359 peridotite wall rock. This interpretation is further supported by the fact that SMI are
360 distributed throughout the entire grains in which they occur (Fig. 2b), thus eliminating the
361 possibility that the melt fractionated some of the host mineral prior to entrapment (as it was
362 observed by Zajacz et al. 2007 in case of SMIs in olivine). Liptai et al. (2017) concluded that
363 the reacting melt was most likely a mafic melt with an asthenospheric origin, similar to the
364 host basalt, but with a slightly different composition. With the chemical compositions
365 obtained by SEM-EDX, characteristics of this melt can be further refined.

366 The most striking compositional feature is the enrichment of FeO in the daughter
367 minerals (i.e., clinopyroxene, amphibole, mica and spinel; Table 3). Iron appears to be the
368 best geochemical proxy to distinguish wall clinopyroxene from the host clinopyroxene, as the
369 former contains significantly higher Fe contents than the latter (Fig. 7; Table 3). The high FeO
370 concentrations in mica result in annite-like compositions. This is strikingly different from the

371 phlogopites described from SMI found in the southern part of the NGVF by Szabó et al.
372 (1996); however, those inclusions have been interpreted to represent a subduction-related
373 melt, and are only present in olivine in xenoliths from the southern part of the volcanic field.
374 Minor FeO is detectable in the glass of SMI_R and SMI_U (Table 3) as well. Overall, these
375 compositions agree well with the Fe-rich nature of the metasomatizing melt associated with
376 formation of the wehrlite suite (Patkó et al. 2020). However, it should be noted that the
377 accompanying Mn- and Ti-enrichment observed in the rock-forming silicates and spinel
378 (Liptai et al. 2017), respectively, is not reflected in the composition of crystallized phases in
379 the SMI. This may be because Mn is only present in very low amounts and was below
380 detection limit with SEM-EDX, and enrichment of Ti may not be that dominant as it only
381 occurred in spinel, but not in clinopyroxene in the affected xenoliths (Liptai et al. 2017).
382 Bulk compositions, both for the four SMI analyzed with SEM-EDX and for the eight
383 additional SMI analyzed with LA-ICP-MS, show generally low alkali contents along with a
384 variability in SiO_2 that places them into compositional fields ranging from basaltic andesite
385 and trachyandesite through basalt to picrobasalt and basanite in the TAS diagram (Le Bas et
386 al. 1986) (Fig. 8). Note that compositions of SMI determined by mass balance calculation
387 have much less variability than those obtained by LA-ICP-MS, which show lower SiO_2 and
388 total alkali contents. The greater compositional variability compared to SEM-EDX analyses,
389 and the general consideration that LA-ICP-MS has lower accuracy for major elements, would
390 suggest that a basaltic andesite/trachyandesite – basalt composition is the best estimate for the
391 composition of the trapped melt. This differs somewhat from the composition of the host
392 magma (Fig. 8), which is a basanite with higher total alkali and lower SiO_2 contents and an
393 overall limited variability among the different localities of the Nógrád-Gömör Volcanic Field
394 (Embey-Isztin et al. 1993; Dobosi et al. 1995; Dobosi and Jenner 1999). The difference is also
395 observed when compared to the estimated primitive composition of the host basalt (Zajacz et

al. 2007), which plots in the basalt field with lower total alkali- and slightly lower SiO_2-contents (Fig. 8).

The production of basaltic melts with small changes in composition depending on their age throughout the Nógrád-Gömör Volcanic Field has been previously observed by Dobosi et al. (1995). The dominant change observed by these workers was an increase in trace elements (Zr, Nb), and to a lesser extent SiO_2 and total alkali contents. Furthermore, the melt represented by the SMI probably had a different evolution, as it resided in the upper mantle and reacted with the wall rock, instead of undergoing a rapid ascent to the surface like the host magma. Such a reaction is considered to be responsible for forming the wehrlites. Patkó et al. (2020) have established that the metasomatizing melt dissolves orthopyroxene and crystallizes clinopyroxene and olivine, while becoming more intermediate in composition. It is, therefore, suggested that this evolved melt was trapped in the SMI.

Origin of the trapped melt based on trace element composition

Because of the analytical uncertainties resulting from low concentrations, only inclusions with Y/Yb = ~10 (an empirical ratio for mantle environment; McDonough and Sun 1995; Salters and Stracke 2004) were used (SMI_9, SMI_10, SMI_12, SMI_13, SMI_16; Fig. 6; Table 4) during averaging SMI compositions to estimate the composition of the trapped melt. Trace-element patterns of the SMI compared with the compositions of amphiboles with intraplate origin formed during different metasomatic events in the NGVF upper mantle (Group IB and IIB of Liptai et al. (2017) are shown on Fig. 9. Regarding the incompatible trace elements, SMI compositions usually fall between the most enriched amphiboles in Group IB and Group IIB xenoliths. Note that the Group IIB xenolith that contains amphibole is a different sample from the one containing the SMI (Liptai et al. 2017). Although Nb and

Ta are significantly more abundant in the amphibole of the most enriched Group IB xenoliths (Fig. 9a) than in the SMI, their REE+Y patterns show good agreement. However, at equilibrium, amphibole/melt partitioning of these trace elements would not allow these elements to be more enriched in amphibole compared to the melt as the relevant distribution coefficients are less than 1 (Adam and Green 1994; LaTourrette et al. 1995; Dalpé and Baker 2000). This can be explained if the Group IB amphiboles are linked to a different metasomatic event, one with an enrichment of U-Th-Nb-Ta in the reacting melt (Liptai et al. 2017), whereas the SMI represent a different melt that was responsible for the wehrlitic metasomatism.

Trace element patterns of the SMI are generally in good agreement with those of the host basalt (Fig. 9c, d), having an OIB character (Dobosi et al. 1995), but the trapped melt appears slightly less fertile, as depicted by depletion in Ba, Nb (Ta), La, Ce, Hf and Zr (Fig. 9c). The high concentrations of incompatible trace elements in the host basalt may be explained by crystallization of olivine and clinopyroxene (fractionation), thus enriching the remaining melt in incompatible trace elements before eruption (Embey-Isztin et al. 1993; Dobosi et al. 1995; Zajacz et al. 2007). This is supported by the calculated composition of the NGVF basalt before fractionation and crustal assimilation (Zajacz et al. 2007), which shows a better agreement with the analyzed SMI (Fig. 9c). Alternatively, the trapped melt may have followed a different evolution path; i.e., reaction with the peridotite and consuming orthopyroxene while crystallizing clinopyroxene and olivine (Patkó et al. 2020), as mentioned earlier.

To constrain the origin of the trapped melt, the equilibrium melting model of Zajacz et al. (2007) was applied to the studied SMI compositions (Fig. 10). This model is based on calculations of Nb and Y in the partial melts for spinel lherzolite and garnet lherzolite sources with different modal clinopyroxene/garnet ratios. Bulk source compositions were determined

using the primitive mantle composition of McDonough and Sun (1995) and mineral-melt partition coefficients from garnet lherzolite melting experiments at pressures between 2.8–3.2 GPa by Salters et al. (2002). Based on the model, Nb is a good indicator for the degree of partial melting, and Y generally indicates the presence of garnet in the source. Furthermore, these elements are in sufficiently high abundances in the SMI to be analyzed with limited uncertainty, and they are considered insensitive to fluid metasomatism in the source. Based on this model (Fig. 10), the melt trapped in the SMI was produced by ~ 2 % melting of a garnet lherzolite, with a clinopyroxene/garnet ratio of ~ 1. The source appears to be slightly more garnet-rich than the calculated parental melt of the Nógrád-Gömör cumulate xenoliths (Zajacz et al. 2007) and the average composition of the host basalt (Fig. 10). However, the latter is already modified due to olivine and clinopyroxene fractionation (Dobosi et al. 1995) and partial crustal assimilation (Zajacz et al. 2007).

In summary, the geochemical characteristics of the melt represented by the SMI point to an OIB-type intraplate melt, with an origin similar to other basaltic magmas present in the region. The observed differences in geochemistry (higher SiO_2 and lower incompatible trace element content compared to the host basalt) can be explained by the combined effects of several possible factors: (1) small differences in the source composition and in the degree of partial melting, (2) fractionation of the host basalt, and (3) evolution of the metasomatic melt via reaction with the peridotite wall-rock prior to entrapment.

Post-entrapment processes

The partially crystallized nature of the SMI in the studied xenolith (Fig. 2c, d) suggests that precipitation of daughter minerals occurred in a slowly cooling environment (Fig. 11a-c). The beginning of crystallization is in many cases a non-equilibrium process. Due to

heterogeneous nucleation on the inclusion wall only the host mineral crystallizes initially, even if the melt is saturated with other phases (e.g., Frezzotti et al. 1991). Consequently, clinopyroxene was the first mineral to crystallize on the inclusion wall. Precipitation of volatile-free phases leads to an increase in the concentration of volatile components in the residual melt, and eventually to crystallization of volatile-bearing daughter phases (Frezzotti 2001) such as amphibole, apatite and mica. The presence of glass in the SMI indicates that rapid cooling interrupted the crystallization process, which is interpreted to have occurred during and/or after ascent to the surface.

As a result of crystallization of mostly non-volatile-bearing phases in the SMI the volatile content of the melt increases, as noted above. At the same time, the pressure in the SMI is decreasing as crystallization proceeds owing to the density (molar volume) differences between the crystal phases and the melt. Stated differently, the partial molar volume of, for example, clinopyroxene in the melt is larger than the molar volume of the clinopyroxene phase that is crystallizing from that melt. Because of this, the pressure in the SMI decreases, favoring the exsolution of volatiles from the melt. The density of the CO_2 bubble may be estimated based on the distance between the peaks of the Fermi diad in the Raman spectrum of CO_2 (Rosso and Bodnar 1995). To calculate the density of the CO_2-bubble, the experimentally developed densimeters of Fall et al. (2011) and Wang et al. (2011) were applied, while recognizing that one should ideally use a densimeter developed for the instrument which analyzed the samples in order to minimize errors (Lamadrid et al. 2017). Since the peak shifts are very similar in the three inclusions, the resulting densities (0.38–0.39 and 0.36–0.37 g/cm^3 with the two densimeters; Table 1) are almost identical. We note that the CO_2 bubbles were analyzed at room temperature, and the resulting densities are in the "forbidden region" because they represent densities that are between the density of CO_2 liquid and CO_2 vapor at room temperature (see Table 1 of Wang et al., 2011). However, repeated

496 analyses of the CO_2 bubbles at 40°C yielded the same results within error. We interpret this to
497 indicate that the temperature of the CO_2 in the bubbles was slightly elevated by interaction
498 with the laser, resulting in homogenization of the CO_2 phases during the analysis, thus
499 resulting in correct densities. In addition to the similar densities of all bubbles, their volume
500 proportions in the analyzed SMI are in the same range (7–14 vol. %; Table 2), and the
501 remaining inclusions in the sample have roughly similar-sized bubbles. Both the identical CO_2
502 densities and the similar volume proportions of the bubbles support the interpretation that the
503 CO_2 was completely dissolved in the trapped melt and that the bubbles were most likely
504 formed via post-entrapment devolatilization during ascent to the surface.
505 The density of CO_2 in the vapor bubble of SMI can be used to estimate the weight
506 proportion of CO_2 in the trapped melt using mass balance approach. The CO_2 content of the
507 trapped melt, in turn, may be used to estimate a minimum pressure of trapping of the SMI.
508 For the mass balance calculations, volume properties acquired with FIB-SEM analyses were
509 used, along with densities of the daughter minerals or the endmembers closest in composition
510 (diopside, pargasite, annite, hercynite and pyrrhotite for clinopyroxene, amphibole, mica,
511 spinel and sulfide, respectively), CO_2 densities obtained from Raman analysis of the vapor
512 bubbles, and an average glass density of Stolper and Walker (1980). The resulting mass
513 proportion of CO_2 in SMI_2, SMI_3, SMI_R and SMI_U is estimated to be 2.1, 1.9, 1.7 and
514 1.0 wt.%, respectively. CO_2 concentrations determined in this manner represent minimum
515 values, as some additional CO_2 is contained in the glass phase. Nevertheless, Moore et al.
516 (2015; 2018), Moore and Bodnar (2019), and Wallace et al. (2015) have shown that the
517 majority of the CO_2 is contained in the vapor bubble in silicate melt inclusions, with the vapor
518 bubble containing > 90 % of the total CO_2 in many SMI. We note that the glass is not
519 completely homogeneous in the SMI, which is evidenced by numerous dark spots observable
520 on the BSE image (Fig. 3b, 5). Analyses of these spots did not reveal any compositional

difference from the surrounding glass. Given their dark color, the spots may represent tiny gas bubbles that froze in the glass before they could coalesce with the main bubble. The weight proportions of CO_2 determined here are somewhat lower than values reported by Zajacz et al. (2007) for the parental melt of NGVF cumulates (2.20 – 2.55 wt. %), and fall within the range proposed for more oxidized primary OIB magmas (0.2 - 3.0 wt. %; Herzberg and Asimow 2008).

Ignoring the contributions of other minor volatile components as described below, the minimum depth of trapping of the SMI may be estimated based on the CO_2 abundances of 1.0 to 2.1 wt. % reported above. According to Mysen et al. (1975), the solubility of CO_2 in a tholeiitic melt at 1650°C varies from ~1 wt. % at 0.5 GPa to ~2 wt. % at 1.5 GPa. These workers also showed that the solubility changes little with temperature at temperatures <1500°C at 3 GPa, although data for lower temperatures are not included. Assuming that these results for a tholeiitic melt reasonably approximate the behavior of the SMI studied here suggests that the SMI were trapped at a minimum pressure of 0.5 – 1.5 GPa. These values are in agreement with the depths of 40-50 km and pressures of 1.3 – 1.6 GPa where wehrlitic metasomatism occurred in the NGVF (Patkó et al. 2020). The presence of other volatile-bearing phases in the SMI of this study suggests that the original composition of the volatile bubble did not consist exclusively of CO_2. Crystals growing inside the bubble can be interpreted as having formed during a late crystallization process, following the exsolution of the volatiles from the residual melt (Esposito et al. 2016). Crystals that form in a fluid or melt inclusion not by precipitation directly from the trapped fluid but, rather as a result of interaction between the volatile phase and either the host mineral, glass/melt, or previously-formed daughter minerals are referred to as “step-daughter minerals” (Svensen et al. 1999). In the studied inclusions, anhydrite and barite (where present) are always located on the boundary between the bubble and the glass (Fig. 4, 5). Although they appear to have grown at

546 the expense of the glass, Frezzotti and Touret (2014) suggested that anhydrite can form during
547 the latest stages of ascent. The close association with barite (SMI_2 on Fig. 4) implies a
548 common genesis. Sulphur is a common component in the volatile phase of mantle fluids (e.g.,
549 Andersen et al. 1984; Andersen and Neumann 2001; Esposito et al. 2016; Aradi et al. 2019),
550 and it can explain the crystallization of these minerals as the glass contains sufficient amounts
551 of Ca (Table 3) and probably Ba as well.

552 In addition to sulfates, mica also appears on the boundary between the gas bubble and
553 the glass (BSE images on Fig. 3b and 5), with the exception of SMI_U, where only one of the
554 two mica flakes is in contact with the bubble (Fig. 3b). In all four SMI, mica appears to grow
555 partly inside the bubble. This suggests that mica also formed at a late stage, following the
556 exsolution of the volatile phase. Furthermore, mica may contain a significant amount of OH
557 in its structure. Although this could not be determined by the FIB-SEM analyses, the lack of
558 detected F and Cl in mica may suggest that the only volatile component occupying the OH
559 site is OH, which could have come from H_2O in the bubble. The enriched structural hydroxyl
560 content of clinopyroxenes in xenolith NFL1327 (265 ppm) compared to the average of that in
561 other xenoliths from the same locality (140 ppm) (Patkó et al. 2019) further suggests that the
562 metasomatic agent included water as a component.

563 Silicate melts transition from the melt (fluid) stage to the glass (solid) over a few tens of
564 degrees, and the higher the cooling rate, the higher the temperature at which this transition
565 will occur (Mysen and Richet 2005). As was shown by Szabó and Bodnar (1996), the NGVF
566 basalts entraining the xenoliths ascended from the depth of entrapment to the surface in a
567 relatively short time (~37.5 hours). This suggests that the cooling rate may only have changed
568 from slow to fast after the eruption. Note that there can be significant differences in the
569 cooling rate in a basaltic lava flow depending not only on time but also on the distance from
570 the contact surface (e.g., Griffiths and Fink 1993). Nevertheless, in the case of the studied

571 xenolith, the time between bubble formation and the solidification of the residual melt was
572 sufficient for sulfate and mica to crystallize (Fig. 11d-f).
573
574 **Implications**
575
576 Our study has three major implications. First, it was found that silicate melt inclusions
577 (SMI) hosted in clinopyroxene in the studied NGVF xenolith represent a metasomatic melt
578 that played an important role in the geochemical evolution of the upper mantle of the northern
579 Pannonian Basin. Compositional features of the trapped melt include an enrichment in FeO
580 and a trace-element pattern similar to the host basalt. Based on this, the melt can be linked to
581 the last metasomatic event recorded in the geochemistry of the NGVF upper mantle, which
582 resulted in the formation of wehrlites by alteration of lherzolites. The metasomatizing melt
583 was an OIB-type mafic melt of intraplate origin, with a genesis similar to that of the alkali
584 basalt hosting the xenoliths, i.e., very small degree (~2 %) of partial melting of a garnet
585 lherzolite source.
586 Second, different post-entrapment processes were identified based on the morphology,
587 composition and arrangements of daughter minerals, residual glass and CO_2-bubble within the
588 SMI. The very similar densities and volume proportions of the CO_2-bubbles in all SMI
589 suggest that the CO_2 exsolved from the residual melt after the entrapment. Following
590 exsolution of the bubble, small mica and sulfate crystals formed on the bubble-melt boundary.
591 This suggests that the volatile phase contained sulfur and possibly H_2O, in addition to CO_2.
592 Third, our study has shown that a much better understanding of the geochemistry and
593 3D distribution of phases in SMI is obtained by applying several different complementary
594 analytical methods to interrogate SMI. The FIB-SEM-EDX system is a powerful tool for
595 acquiring precise volume proportions and compositions of daughter phases during a single set

596 of measurements. Analyzing the whole inclusion volume is especially useful if there are
597 several smaller daughter minerals that cannot all be exposed within the same plane for
598 analysis.
599
600 **Acknowledgements**
601
602 The authors owe thanks to László E. Aradi for his help with Raman spectroscopy, as
603 well as to Ábel Szabó and Zoltán Dankházi for their assistance during FIB-SEM analyses. We
604 are grateful to the two anonymous reviewers whose comments significantly improved our
605 manuscript. This research was financially supported by Macquarie University international
606 PhD scholarship, and project and travel funding from ARC Centre of Excellence for Core to
607 Crust Fluid Systems (CCFS) to N. Liptai. Further support was provided by a Bolyai János
608 Postdoctoral Research Fellowship of the Hungarian Academy of Sciences to M. Berkesi, and
609 the MTA CSFK Lendület Pannon LitH_2Oscope Research Group. L. Patkó was supported by
610 the GINOP-2.3.2-15-2016-00009 research program. Cs. Szabó was supported by the ELTE
611 Institutional Excellence Program 1783-3/2018/FEKUTSRAT (Hungary).
612 This is the 95th publication of the Lithosphere Fluid Research Lab (LRG), contribution
613 XXXX from the ARC Centre of Excellence for Core to Crust Fluid Systems
614 (www.ccfs.mq.edu.au) and XXXX from the GEMOC Key Centre (www.gemoc.mq.edu.au).
615
616
617 **References**
618
619 Adam, J., and Green, T., 1994. The effects of pressure and temperature on the partitioning of
620 Ti, Sr and REE between amphibole, clinopyroxene and basanitic melts. Chemical Geology,
621 117, 219-233.

Andersen, T., and Neumann, E.-R., 2001. Fluid inclusions in mantle xenoliths. Lithos, 55, 301-320.

Andersen, T., O'Reilly, S.Y., and Griffin, W.L., 1984. The trapped fluid phase in upper mantle xenoliths from Victoria, Australia: implications for mantle metasomatism. Contributions to Mineralogy and Petrology, 88, 72-85. 10.1007/bf00371413

Aradi, L.E., Berkesi, M., and Szabó, C., 2019. Composition and origin of upper-mantle fluids, based on fluid inclusions in amphibole-rich harzburgite xenoliths from the Styrian Basin (in Hungarian with English abstract). Bulletin of the Hungarian Geological Society, 149, 35-49.

Bada, G., Horváth, F., Dövényi, P., Szafián, P., Windhoffer, G., and Cloetingh, S., 2007. Present-day stress field and tectonic inversion in the Pannonian basin. Global and Planetary Change, 58, 165-180. http://doi.org/10.1016/j.gloplacha.2007.01.007

Balogh, K., Árva-Sós, E., and Pécskay, Z., 1986. K/Ar dating of post Sarmatian alkali basaltic rocks in Hungary. Acta Mineralogie et Petrographie Szeged, 28, 75-93.

Balogh, K., Mihaliková, A., and Vass, D., 1981. Radiometric dating of basalts in southern and central Slovakia. Západné Karpaty, séria Geológia, 7, 113-126.

Berkesi, M., Guzmics, T., Szabó, C., Dubessy, J., Bodnar, R.J., Hidas, K., and Ratter, K., 2012. The role of CO2-rich fluids in trace element transport and metasomatism in the lithospheric mantle beneath the Central Pannonian Basin, Hungary, based on fluid inclusions in mantle xenoliths. Earth and Planetary Science Letters, 331, 8-20. https://doi.org/10.1016/j.epsl.2012.03.012

Bodnar, R.J., and Frezzotti, M.L., 2020. Microscale Chemistry: Raman Analysis of Fluid and Melt Inclusions. Elements, 16, 93-98. 10.2138/gselements.16.2.93

Créon, L., Levresse, G., Remusat, L., Bureau, H., and Carrasco-Núñez, G., 2018. New method for initial composition determination of crystallized silicate melt inclusions. Chemical Geology, 483, 162-173. https://doi.org/10.1016/j.chemgeo.2018.02.038

Csontos, L., 1995. Tertiary tectonic evolution of the Intra-Carpathian area: a review. Acta Vulcanologica, 7, 1-13.

Csontos, L., Nagymarosy, A., Horváth, F., and Kovác, M., 1992. Tertiary evolution of the Intra-Carpathian area: A model. Tectonophysics, 208, 221-241. https://doi.org/10.1016/0040-1951(92)90346-8

Dalpé, C., and Baker, D.R., 2000. Experimental investigation of large-ion-lithophile-element-, high-field-strength-element-and rare-earth-element-partitioning between calcic amphibole and basaltic melt: the effects of pressure and oxygen fugacity. Contributions to Mineralogy and Petrology, 140, 233-250.

Dobosi, G., Fodor, R.V., and Goldberg, S.A., 1995. Late-Cenozoic alkali basalt magmatism in Northern Hungary and Slovakia: petrology, source compositions and relationship to tectonics., 7, 199-207.

Dobosi, G., and Jenner, G., 1999. Petrologic implications of trace element variation in clinopyroxene megacrysts from the Nograd volcanic province, north Hungary: a study by laser ablation microprobe-inductively coupled plasma-mass spectrometry. Lithos, 46, 731-749.

Duan, X., Sun, H., Yang, W., Su, B., Xiao, Y., Hou, Z., and Shi, H., 2014. Melt–peridotite interaction in the shallow lithospheric mantle of the North China Craton: evidence from melt inclusions in the quartz-bearing orthopyroxene-rich websterite from Hannuoba. International Geology Review, 56, 448-472.

Embey-Isztin, A., Downes, H., James, D.E., Upton, B.G.J., Dobosi, G., Ingram, G.A., Harmon, R.S., and Scharbert, H.G., 1993. The petrogenesis of Pliocene alkaline volcanic rocks from the Pannonian Basin, Eastern Central Europe. Journal of Petrology, 34, 317-343. https://doi.org/10.1093/petrology/34.2.317

Esposito, R., Lamadrid Hector, M., Redi, D., Steele-MacInnis, M., Bodnar Robert, J., Manning Craig, E., De Vivo, B., Cannatelli, C., and Lima, A., 2016. Detection of liquid H2O in vapor bubbles in reheated melt inclusions: implications for magmatic fluid composition and volatile budgets of magmas?, American Mineralogist, pp. 1691-1695. 10.2138/am-2016-5689

Fall, A., Tattitch, B., and Bodnar, R.J., 2011. Combined microthermometric and Raman spectroscopic technique to determine the salinity of H2O–CO2–NaCl fluid inclusions based on clathrate melting. Geochimica et Cosmochimica Acta, 75, 951-964. https://doi.org/10.1016/j.gca.2010.11.021

Fermi, E., 1931. Über den Ramaneffekt des Kohlendioxyds. Zeitschrift für Physik, 71, 250-259. 10.1007/bf01341712

Frezzotti, M.-L., and Touret, J.L., 2014. CO2, carbonate-rich melts, and brines in the mantle. Geoscience Frontiers, 5, 697-710.

Frezzotti, M.L., 2001. Silicate-melt inclusions in magmatic rocks: applications to petrology. Lithos, 55, 273-299.

Frezzotti, M.L., De Vivo, B., and Clocchiatti, R., 1991. Melt-mineral-fluid interactions in ultramafic nodules from alkaline lavas of Mount Etna (Sicily, Italy): Melt and fluid inclusion evidence. Journal of Volcanology and Geothermal Research, 47, 209-219. https://doi.org/10.1016/0377-0273(91)90001-G

Frezzotti, M.L., Tecce, F., and Casagli, A., 2012. Raman spectroscopy for fluid inclusion analysis. Journal of Geochemical Exploration, 112, 1-20. http://dx.doi.org/10.1016/j.gexplo.2011.09.009

Griffiths, R.W., and Fink, J.H., 1993. Effects of surface cooling on the spreading of lava flows and domes. Journal of Fluid Mechanics, 252, 667-702.

Halter, W.E., Pettke, T., Heinrich, C.A., and Rothen-Rutishauser, B., 2002. Major to trace element analysis of melt inclusions by laser-ablation ICP-MS: methods of quantification. Chemical Geology, 183, 63-86.

Harangi, S., Downes, H., Kósa, L., Szabó, C., Thirlwall, M.F., Mason, P.R.D., and Mattey, D., 2001. Almandine Garnet in Calc-alkaline Volcanic Rocks of the Northern Pannonian Basin (Eastern-Central Europe): Geochemistry, Petrogenesis and Geodynamic Implications. J. Petrology, 42, 1813-1843.

Herzberg, C., and Asimow, P.D., 2008. Petrology of some oceanic island basalts: PRIMELT2. XLS software for primary magma calculation. Geochemistry, Geophysics, Geosystems, 9.

Hidas, K., Guzmics, T., Szabó, C., Kovács, I., Bodnar, R.J., Zajacz, Z., Nédli, Z., Vaccari, L., and Perucchi, A., 2010. Coexisting silicate melt inclusions and H2O-bearing, CO2-rich fluid inclusions in mantle peridotite xenoliths from the Carpathian-Pannonian region (central Hungary). Chemical Geology, 274, 1-18. https://doi.org/10.1016/j.chemgeo.2010.03.004

Horváth, F., 1993. Towards a mechanical model for the formation of the Pannonian basin. Tectonophysics, 226, 333-357. https://doi.org/10.1016/0040-1951(93)90126-5

Horváth, F., and Cloetingh, S., 1996. Stress-induced late-stage subsidence anomalies in the Pannonian basin. Tectonophysics, 266, 287-300. https://doi.org/10.1016/S0040-1951(96)00194-1

Hurai, V., Danišík, M., Huraiová, M., Paquette, J.-L., and Ádám, A., 2013. Combined U/Pb and (U–Th)/He geochronometry of basalt maars in Western Carpathians: implications for age of intraplate volcanism and origin of zircon metasomatism. Contributions to Mineralogy and Petrology, 166, 1235-1251. https://doi.org/10.1007/s00410-013-0922-1

Konecný, V., Lexa, J., Balogh, K., and Konecný, P., 1995. Alkali basalt volcanism in Southern Slovakia: volcanic forms and time evolution. Acta Vulcanologica, 7, 167-171.

Lafuente, B., Downs, R.T., Yang, H., and N, S., 2015. The power of databases: The RRUFF project, in: Armbruster, T., Danisi, R.M. (Eds.), Highlights in Mineralogical Crystallography. Walter de Gruyter, Berlin, Germany, pp. 1-29.

Lamadrid, H., Moore, L., Moncada, D., Rimstidt, J., Burruss, R., and Bodnar, R., 2017. Reassessment of the Raman CO2 densimeter. Chemical Geology, 450, 210-222.
LaTourrette, T., Hervig, R.L., and Holloway, J.R., 1995. Trace element partitioning between amphibole, phlogopite, and basanite melt. Earth and Planetary Science Letters, 135, 13-30.
Le Bas, M.J., Le Maitre, R.W., Streckeisen, A., and Zanettin, B., 1986. A chemical classification of volcanic rocks based on the total alkali-silica diagram. Journal of Petrology, 27, 745-750.
Lexa, J., Seghedi, I., Németh, K., Szakács, A., Konečný, V., Pécskay, Z., Fülöp, A., and Kovacs, M., 2010. Neogene-Quaternary Volcanic forms in the Carpathian-Pannonian Region: a review. Central European Journal of Geosciences, 2, 207-270. DOI 10.2478/v10085-010-0024-5
Lin, F., Sum, A.K., and Bodnar, R.J., 2007. Correlation of methane Raman ν1 band position with fluid density and interactions at the molecular level. Journal of Raman Spectroscopy, 38, 1510-1515. 10.1002/jrs.1804
Liptai, N., Patkó, L., Kovács, I.J., Hidas, K., Pintér, Z., Jeffries, T., Zajacz, Z., O'Reilly, S.Y., Griffin, W.L., Pearson, N.J., and Szabó, C., 2017. Multiple metasomatism beneath the Nógrád–Gömör Volcanic Field (Northern Pannonian Basin) revealed by upper mantle peridotite xenoliths. Journal of Petrology, 58, 1107-1144.
https://doi.org/10.1093/petrology/egx048
Longerich, H.P., Jackson, S.E., and Günther, D., 1996. Inter-laboratory note. Laser ablation inductively coupled plasma mass spectrometric transient signal data acquisition and analyte concentration calculation. Journal of Analytical Atomic Spectrometry, 11, 899-904.
McDonough, W.F., and Sun, S.-S., 1995. The composition of the Earth. Chemical Geology, 120, 223-253.
Moore, L.R., and Bodnar, R.J., 2019. A pedagogical approach to estimating the CO₂ budget of magmas. Journal of the Geological Society, 176, 398-407. 10.1144/jgs2018-094
Moore, L.R., Gazel, E., Tuohy, R., Lloyd, A.S., Esposito, R., Steele-MacInnis, M., Hauri, E.H., Wallace, P.J., Plank, T., and Bodnar, R.J., 2015. Bubbles matter: An assessment of the contribution of vapor bubbles to melt inclusion volatile budgets. American Mineralogist, 100, 806-823.
Moore, L.R., Mironov, N., Portnyagin, M., Gazel, E., and Bodnar, R.J., 2018. Volatile contents of primitive bubble-bearing melt inclusions from Klyuchevskoy volcano, Kamchatka: Comparison of volatile contents determined by mass-balance versus experimental homogenization. Journal of Volcanology and Geothermal Research.
https://doi.org/10.1016/j.jvolgeores.2018.03.007
Mutchler, S., Fedele, L., and Bodnar, R.J., 2008. Analysis Management System (AMS) for reduction of laser ablation ICPMS data, in: Sylvester, P. (Ed.), Laser-Ablation-ICPMS in the Earth Sciences: Current Practices and Outstanding Issues. Mineralogical Association of Canada, Vancouver, BC, pp. 318-327.
Mysen, B.O., Arculus, R., and Eggler, D.H., 1975. Solubility of carbon dioxide in melts of andesite, tholeiite, and olivine nephelinite composition to 30 kbar pressure. Contributions to Mineralogy and Petrology, 53, 227-239.
Mysen, B.O., and Richet, P., 2005. Silicate glasses and melts: Properties and structure. Elsevier, New York.
Newton, R.C., and Manning, C.E., 2004. Solubility of anhydrite, CaSO4, in NaCl–H2O solutions at high pressures and temperatures: applications to fluid–rock interaction. Journal of Petrology, 46, 701-716.
Patkó, L., Liptai, N., Aradi, L., Bodnar, R., Sendula, E., Kovács, I., Klébesz, R., and Szabó, C., 2018. Deciphering mantle metasomatism using silicate melt inclusions beneath the

Nógrád-Gömör Volcanic Field (Northern Pannonian Basin). Geophysical Research Abstracts, 20, EGU2018-2785.

Patkó, L., Liptai, N., Aradi, L.E., Klébesz, R., Sendula, E., Bodnar, R.J., Kovács, I.J., Hidas, K., Cesare, B., Novák, A., Trásy, B., and Szabó, C., 2020. Metasomatism-induced wehrlite formation in the upper mantle beneath the Nógrád-Gömör Volcanic Field (Northern Pannonian Basin): Evidence from xenoliths. Geoscience Frontiers, in press. https://doi.org/10.1016/j.gsf.2019.09.012

Patkó, L., Liptai, N., Kovács, I.J., Aradi, L.E., Xia, Q.-K., Ingrin, J., Mihály, J., O'Reilly, S.Y., Griffin, W.L., Wesztergom, V., and Szabó, C., 2019. Extremely low structural hydroxyl contents in upper mantle xenoliths from the Nógrád-Gömör Volcanic Field (northern Pannonian Basin): Geodynamic implications and the role of post-eruptive re-equilibration. Chemical Geology, 507, 23-41. https://doi.org/10.1016/j.chemgeo.2018.12.017

Qin, Z., Lu, F., and Anderson, A.T., 1992. Diffuse reequilibration of melt and fluid inclusions. American Mineralogist, 77, 565-576.

Richard, A., Morlot, C., Créon, L., Beaudoin, N., Balistky, V.S., Pentelei, S., Dyja-Person, V., Giuliani, G., Pignatelli, I., and Legros, H., 2018. Advances in 3D imaging and volumetric reconstruction of fluid and melt inclusions by high resolution X-ray computed tomography. Chemical Geology, in press.

Ritchie, N.W., Newbury, D.E., and Davis, J.M., 2012. EDS measurements of X-ray intensity at WDS precision and accuracy using a silicon drift detector. Microscopy and Microanalysis, 18, 892-904.

Roedder, E., 1983. Geobarometry of ultramafic xenoliths from Loihi Seamount, Hawaii, on the basis of CO2 inclusions in olivine. Earth and Planetary Science Letters, 66, 369-379.

Roedder, E., 1984. Fluid inclusions. Mineralogical Society of America.

Rosso, K.M., and Bodnar, R.J., 1995. Microthermometric and Raman spectroscopic detection limits of CO2 in fluid inclusions and the Raman spectroscopic characterization of CO2. Geochimica et Cosmochimica Acta, 59, 3961-3975. https://doi.org/10.1016/0016-7037(95)94441-H

Salters, V.J., Longhi, J.E., and Bizimis, M., 2002. Near mantle solidus trace element partitioning at pressures up to 3.4 GPa. Geochemistry, Geophysics, Geosystems, 3, 1-23.

Salters, V.J., and Stracke, A., 2004. Composition of the depleted mantle. Geochemistry, Geophysics, Geosystems, 5.

Schiano, P., and Bourdon, B., 1999. On the preservation of mantle information in ultramafic nodules: glass inclusions within minerals versus interstitial glasses. Earth and Planetary Science Letters, 169, 173-188.

Schiano, P., Clocchiatti, R., Bourdon, B., Burton, K., and Thellier, B., 2000. The composition of melt inclusions in minerals at the garnet–spinel transition zone. Earth and Planetary Science Letters, 174, 375-383.

Schiano, P., Clocchiatti, R., and Joron, J., 1992. Melt and fluid inclusions in basalts and xenoliths from Tahaa Island, Society Archipelago: evidence for a metasomatized upper mantle. Earth and Planetary Science Letters, 111, 69-82.

Stolper, E., and Walker, D., 1980. Melt density and the average composition of basalt. Contributions to Mineralogy and Petrology, 74, 7-12.

Svensen, H., Jamtveit, B., Yardley, B., Engvik, A.K., Austrheim, H.k., and Broman, C., 1999. Lead and bromine enrichment in eclogite-facies fluids: extreme fractionation during lower-crustal hydration. Geology, 27, 467-470.

Szabó, C., and Bodnar, R., 1996. Changing magma ascent rates in the Nógrád-Gömör Volcanic Field Northern Hungary/Southern Slovakia: Evidence from CO2-rich fluid inclusions in metasomatized upper mantle xenoliths. Petrology, 4, 221-230.

Szabó, C., Bodnar, R.J., and Sobolev, A.V., 1996. Metasomatism associated with subduction-related, volatile-rich silicate melt in the upper mantle beneath the Nograd-Gomor volcanic field, northern Hungary/southern Slovakia; evidence from silicate melt inclusions. European Journal of Mineralogy, 8, 881-899.

Szabó, C., Hidas, K., Bali, E., Zajacz, Z., Kovács, I., Yang, K., Guzmics, T., and Török, K., 2009. Melt-wall rock interaction in the mantle shown by silicate melt inclusions in peridotite xenoliths from the central Pannonian Basin (western Hungary). Island Arc, 18, 375-400. DOI 10.1111/j.1440-1738.2009.00672.x

Török, K., 1995. Garnet breakdown reaction and fluid inclusions in a garnet-clinopyroxenite xenolith from Szentbékkálla (Balaton-Highland, Western Hungary). Acta Vulcanologica, 7, 285-290.

Viti, C., and Frezzotti, M.-L., 2000. Re-equilibration of glass and CO2 inclusions in xenolith olivine: A TEM study. American Mineralogist, 85, 1390-1396.

Wallace, P.J., Kamenetsky, V.S., and Cervantes, P., 2015. Melt inclusion CO2 contents, pressures of olivine crystallization, and the problem of shrinkage bubbles. American Mineralogist, 100, 787-794.

Wang, X., Chou, I.M., Hu, W., Burruss, R.C., Sun, Q., and Song, Y., 2011. Raman spectroscopic measurements of CO2 density: Experimental calibration with high-pressure optical cell (HPOC) and fused silica capillary capsule (FSCC) with application to fluid inclusion observations. Geochimica et Cosmochimica Acta, 75, 4080-4093. https://doi.org/10.1016/j.gca.2011.04.028

Wirth, R., 2004. Focused Ion Beam (FIB): A novel technology for advanced application of micro- and nanoanalysis in geosciences and applied mineralogy. European Journal of Mineralogy, 16, 863-876. 10.1127/0935-1221/2004/0016-0863

Zajacz, Z., Kovács, I., Szabó, C., Halter, W., and Pettke, T., 2007. Evolution of mafic alkaline melts crystallized in the uppermost lithospheric mantle: a melt inclusion study of olivine-clinopyroxenite xenoliths, northern Hungary. Journal of Petrology, 48, 853-883. https://doi.org/10.1093/petrology/egm004

Figure captions

Fig. 1. (a) Locations of alkali basalt occurrences that host ultramafic xenoliths in the Carpathian-Pannonian region. SB – Styrian Basin, LHP – Little Hungarian Plain, BBH – Bakony-Balaton Highland, NG – Nógrád-Gömör, PM – Perşani Mountains. (b) Outcrops of alkali basalt and Miocene andesites (with possible mantle origin; Harangi et al. 2001) in the Nógrád-Gömör Volcanic Field (NGVF) and sampling locality (Fil'akovo-Kerčik) of the studied xenolith.

Fig. 2. (a) Scanned thin section image of the studied xenolith, with well-defined olivine-rich and clinopyroxene-rich areas. (b) Transmitted light, plane-polarized photomicrograph of a clinopyroxene grain hosting silicate melt inclusions (SMI). (c) (d) Photomicrographs showing the SMI selected for analyses presented in this study. The images are merged from a set of photos taken in different focal depths.

Fig. 3. (a) Backscattered electron image of the sample volume containing an SMI, prepared for slicing with the focused ion beam (FIB) following the deposition of the Pt-layer and excavating the surrounding trenches (see text for further details). (b) Photomicrograph of SMI_U (transmitted light, plane polarized); numbered dashed lines and corresponding BSE images indicate different stages of the FIB-slicing. (c) Computed 3D volume of SMI_U indicating daughter phases in different colors (without the clinopyroxene, which is thought to be present all along the inclusion wall).

Fig. 4. Selected Raman spectra of daughter phases and the host clinopyroxene (upper); photomicrographs (transmitted light, plane polarized) and Raman spectroscopic maps of three analyzed SMI (lower). Color code: dark blue – amphibole; light blue – wall clinopyroxene; red – apatite; green – sulfates (anhydrite and barite); yellow – glass; purple – CO_2 bubble; white – host clinopyroxene.

Fig. 5. Backscattered electron (BSE) image of a slice of SMI_R with SEM-EDX spectra of the daughter phases present.

Fig. 6. Primitive mantle (McDonough and Sun 1995) normalized multi-element (a) and rare earth element + yttrium (REE+Y) (b) diagrams of bulk SMI analyzed with LA-ICP-MS.

884

885 Fig. 7. Comparison of MgO and FeO concentrations in the rock-forming minerals of the
886 xenoliths and the corresponding minerals in the SMI: (a) wall and host clinopyroxene, both
887 compositions acquired with SEM-EDX; (b) daughter amphibole compared to modal
888 amphibole appearing in the different geochemical groups of the NGVF lherzolite suite (taken
889 from Liptai et al. 2017).

890

891 Fig. 8. Composition of glass and bulk SMI acquired with both LA-ICP-MS and mass
892 balance calculations from major element analyses with SEM-EDX, plotted on the total alkali
893 *vs* SiO_2 (TAS) diagram (Le Bas et al. 1986). Compositions of Nógrád-Gömör alkali basalts
894 (Embey-Isztin et al. 1993; Dobosi et al. 1995) and their estimated primitive composition
895 (Zajacz et al. 2007) are plotted, with fields for compositions of SMI found in cumulates
896 (Zajacz et al. 2007) and 'basaltic' SMI in olivine from the southern part of the NGVF (Szabó
897 et al. 1996).

898

899 Fig. 9. a, b – Multielement and REE+Y diagrams of the bulk SMI compositions
900 compared to the metasomatic amphiboles of Group IB and IIB xenoliths; c, d – compared to
901 the average host basalt (Dobosi and Jenner 1999) and the calculated primitive composition of
902 the host basalt (Zajacz et al. 2007). Concentrations are normalized to primitive mantle
903 (McDonough and Sun 1995).

904

905 Fig. 10. Petrogenetic modelling of the origin of the melt trapped in the SMI (Zajacz et
906 al. 2007). Dashed lines represent modelled compositions of partial melts from spinel and
907 garnet lherzolite, respectively, with primitive mantle composition. Numbers in italics refer to
908 the clinopyroxene/garnet ratio in the source region. Dotted lines represent the degree of partial

909 melting expressed in percent melting. Average composition of the host basalt (pink diamond)
910 (Dobosi and Jenner 1999) and the calculated parental melt composition for the cumulates
911 (black square) (Zajacz et al. 2007) are plotted for comparison.
912
913 Fig. 11. Schematic illustration depicting the evolution history of the metasomatic melt,
914 with different stages in the mantle environment and during/after ascent to the surface. Color
915 code for phases within the SMI: yellow – melt; light blue – wall clinopyroxene; dark blue –
916 amphibole; black – spinel; red – apatite; green – sulfates (anhydrite and barite); orange –
917 mica; purple – volatile bubble; brown – glass.
918
919

This is the peer-reviewed, final accepted version for American Mineralogist, published by the Mineralogical Society of America.
The published version is subject to change. Cite as Authors (Year) Title. American Mineralogist, in press.
DOI: https://doi.org/10.2138/am-2020-7292. http://www.minsocam.org/

Table 1. Positions of CO_2 bands and calculated densities (σ indicates reported maximum uncertainties) in three

Inclusion	Position of CO_2 bands (Fermi diad)		Δ Fermi diad	CO_2 density (g/cm^3)	
	upper band	lower band		Fall et al., 2011 (σ=0.025)	Wang et al., 2011 (σ=0.025)
SMI_2	1283.5	1387.0	103.5	0.348	0.355
SMI_R	1284.7	1388.3	103.6	0.393	0.369
SMI_U	1284.7	1388.3	103.6	0.393	0.364

This is the peer-reviewed, final accepted version for American Mineralogist, published by the Mineralogical Society of America.
The published version is subject to change. Cite as Authors (Year) Title. American Mineralogist, in press.
DOI: https://doi.org/10.2138/am-2020-7292. http://www.minsocam.org/

Table 2. Volumetric proportions (vol%) of recognized phases within the analyzed SMI

	SMI_2	SMI_3	SMI_R	SMI_U
Clinopyroxene	12	7.0	19	19
Amphibole	28	32	22	7.5
Mica	0.5	0.2	1.2	9.4
Glass	43	46	45	53
Apatite	-	0.4	0.5	1.9
Spinel	1.6	0.9	1.0	2.3
Sulfide		-	0.2	0.2
Anhydrite	0.2	0.1	0.1	-
Barite	0.1	0.1	-	-
CO_2 bubble	14	13	12	7.3

This is the peer-reviewed, final accepted version for American Mineralogist, published by the Mineralogical Society of America.
The published version is subject to change. Cite as Authors (Year) Title. American Mineralogist, in press.
DOI: https://doi.org/10.2138/am-2020-7292. http://www.minsocam.org/

Table 3. Major element compositions of the daughter phases and the whole SMI in wt%

	Amphibole					**Mica**			
	SMI_2	SMI_3		SMI_R	SMI_U	SMI_2	SMI_3	SMI_R	SMI_U
		amp1	amp2						
n	4	2	3	7	1	5	3	2	6
SiO_2	39.7 (1.6)	37.9 (3.2)	39.7 (0.2)	38.5 (0.8)	38.5	34.2 (1.6)	41.5 (0.8)	35.9 (3.3)	35.9 (3.0)
TiO_2	3.48 (0.91)	5.23 (1.50)	4.88 (0.61)	3.89 (0.68)	6.95		1.45 (0.22)	3.33 (1.69)	3.93 (1.16)
Al_2O_3	10.6 (0.6)	10.1 (0.4)	10.1 (0.4)	11.4 (0.5)	10.4	11.1 (0.6)	9.04 (1.04)	10.5 (0.4)	14.2 (1.2)
Cr_2O_3				0.76 (0.07)				3.36 (0.74)	
FeO	14.8 (4.6)	14.8 (2.5)	12.3 (0.6)	12.8 (1.1)	12.4	33.8 (3.6)	25.6 (1.4)	29.1 (9.9)	21.1 (2.8)
MgO	11.6 (1.7)	10.8 (1.1)	11.3 (0.7)	11.6 (0.5)	11.0	2.93 (0.51)	3.82 (0.42)	1.73 (0.65)	7.85 (1.12)
CaO	13.6 (0.3)	15.4 (0.2)	15.8 (1.2)	15.3 (0.5)	15.1	5.19 (1.13)	10.3 (1.6)	7.17 (3.37)	2.37 (0.47)
Na_2O	2.25 (0.53)	1.74 (0.11)	2.13 (0.21)	1.75 (0.17)	1.82	1.84 (0.84)	0.93 (0.06)	0.58 (0.16)	2.53 (1.17)
K_2O	1.55 (0.28)	1.59 (0.26)	1.37 (0.27)	1.55 (0.15)	1.40	7.34 (0.93)	3.86 (0.10)	4.81 (1.98)	8.64 (0.60)
Total	97.5	97.5	97.5	97.5	97.5	96.5	96.5	96.5	96.5

	Clinopyroxene						**Spinel**			
	SMI_2		SMI_3	SMI_R		SMI_U	SMI_2	SMI_3	SMI_R	SMI_U
	wall	host	host	wall	host	host				
n	3	3	6	6	5	2	4	1	6	1
SiO_2	50.2 (2.0)	53.0 (1.1)	49.4 (1.1)	46.0 (1.1)	49.0 (0.9)	49.1 (1)				
TiO_2	1.75 (0.00)	1.09 (0.00)	1.08 (0.55)	1.34 (0.25)	1.15 (0.23)	1.10 (0.02)	1.92 (0.00)	3.74	1.79 (0.09)	
Al_2O_3	5.59 (2.03)	4.78 (0.77)	4.08 (0.39)	6.05 (0.55)	4.23 (0.22)	4.19 (0.42)	7.09 (0.92)	9.54	5.77 (0.83)	43.7
Cr_2O_3			1.36 (0.22)		1.55 (0.20)		11.4 (1.6)	6.33	5.80 (0.72)	3.30
FeO	8.50 (1.31)	2.76 (0.00)	5.81 (0.78)	9.51 (0.72)	6.44 (0.28)	6.18 (0.61)	79.6 (6.1)	80.4	86.6 (3.2)	47.2
MgO	11.3 (2.0)	13.9 (1.0)	12.6 (0.9)	10.4 (0.7)	11.9 (0.3)	11.9 (0.3)				5.81
CaO	22.1 (1.8)	24.0 (1.4)	25.1 (1.5)	25.6 (1.4)	25.5 (0.7)	26.6 (0.5)				
Na_2O	1.66 (0.10)	1.15 (0.17)	0.79 (0.20)	1.03 (0.38)	0.76 (0.32)	0.87 (0.42)				
K_2O				0.49 (0.00)		0.30 (0.00)				
Total	101.10	100.68	100.22	100.42	100.53	100.24	100.01	100.00	99.96	100.00

This is the peer-reviewed, final accepted version for American Mineralogist, published by the Mineralogical Society of America.
The published version is subject to change. Cite as Authors (Year) Title. American Mineralogist, in press.
DOI: https://doi.org/10.2138/am-2020-7292. http://www.minsocam.org/

	Glass							Whole SMI			
	SMI_2		SMI_3	SMI_R		SMI_U		SMI_2	SMI_3	SMI_R	SMI_U
	K-rich	Na-rich	K-rich	Krich	Na-rich	Krich	Na-rich				
n	9	1	3	8	4	7	1				
SiO_2	66.5 (1.7)	59.6	65.5 (1.9)	63.6 (1.3)	52 (1.8)	62.4 (1.9)	57.8	53.2	52.9	51.7	52.1
TiO_2								1.53	2.11	1.40	1.26
Al_2O_3	20.3 (0.5)	18.6	18.4 (0.9)	20.3 (1)	17.4 (1.4)	18.9 (1.8)	17.6	14.3	13.7	14.3	15.0
Cr_2O_3								0.27	0.20	0.32	0.11
FeO					1.65 (0.38)	2.34 (0.94)	3.40	8.36	6.57	7.24	7.50
MgO	0.81 (0.27)	0.66	1.61 (0.60)	1.12 (0.24)	0.84 (0.50)	1.56 (0.56)	1.48	6.22	6.38	6.02	5.55
CaO	1.67 (0.48)	1.55	2.81 (1.12)	2.80 (0.83)	2.74 (1.73)	3.12 (0.78)	2.09	9.06	9.95	11.5	10.6
Na_2O	3.40 (2.03)	12.0	2.97 (1.95)	2.10 (1.15)	15.91 (2.39)	1.28 (0.29)	7.23	2.65	2.36	1.71	1.31
K_2O	2.86 (0.71)	3.10	4.21 (1.07)	5.57 (0.80)	4.92 (0.53)	5.95 (1.43)	5.85	1.87	2.68	3.24	4.29
P_2O_5											0.91
F_2O											0.02
Cl_2O											0.04
Total	95.5	95.5	95.5	95.5	95.5	95.5	95.5	97.5	96.9	97.4	98.6

Notes: standard deviation (1σ) values are shown in brackets where the number of analyses (n) exceeds 1.

This is the peer-reviewed, final accepted version for American Mineralogist, published by the Mineralogical Society of America.
The published version is subject to change. Cite as Authors (Year) Title. American Mineralogist, in press.
DOI: https://doi.org/10.2138/am-2020-7292. http://www.minsocam.org/

Table 4. Trace element compositions of SMI analyzed with LA-ICP-MS (ppm)

	SMI_8		SMI_9		SMI_10		SMI_12		SMI_13		SMI_14		SMI_15		SMI_16	
		3σ		3σ		3σ		3σ		3σ		3σ		3σ		3σ
Ba	530	1	193	1	232	1	228	1	194	1	117	1	227	0	311	1
Nb	86.7	1.9	33.4	1.8	41.0	1.7	39.7	1.8	36.1	1.7	19.6	1.3	32.2	1.4	44.1	1.4
Ta	4.56	0.60	1.74	0.79	2.00	0.36	1.87	0.62	1.81	0.89	0.92	0.32	1.78	0.46	1.93	0.69
La	39.1	1.2	15.9	0.6	17.2	0.9	22.8	0.8	18.9	0.8	16.1	0.7	22.4	1.4	19.3	0.9
Ce	83.8	1.5	44.1	0.0	39.3	1.4	55.1	0.7	46.7	0.0	37.8	1.2	49.4	0.8	42.4	1.0
Sr	865	2	338	2	338	2	407	2	405	2	278	2	367	2	364	2
Pr	9.88	0.82	7.20	1.56	5.71	1.88	6.82	1.31	6.09	1.74	4.91	1.98	5.83	1.59	6.29	1.83
Nd	43.0	2.0	29.9	1.8	24.3	2.8	34.1	1.9	29.6	1.4	16.7	2.0	29.0	2.2	24.4	2.7
Hf	2.38	0.96	1.26	1.05	1.68	1.38	1.41	0.86	1.41	0.66	0.51*	2.87	1.64	1.42	1.61	1.06
Zr	152	2	97.3	1.3	64.7	1.7	96.4	1.2	90.9	1.5	61.0	1.3	99.5	1.5	88.5	2.1
Sm	8.27	1.42	3.62	1.63	5.04	1.30	4.03	0.81	6.96	1.05	3.73	1.84	4.07	1.19	4.39	1.71
Eu	2.05	1.28	1.84	0.79	1.32*	1.72	1.58*	1.63	1.74	1.31	0.99*	1.69	1.12*	2.12	1.33*	2.37
Gd	5.49	1.20	4.23	1.88	4.13	1.86	5.93	0.62	5.46	0.92	3.28	2.34	4.44	1.96	3.73	1.54
Tb	0.60*	3.09	0.97*	1.71	0.39*	2.23	0.68*	1.54	0.60*	0.77	0.33*	2.87	0.25*	3.55	0.83*	0.91
Ti	12034	4	8563	3	10722	3	6544	4	7069	4	3043	6	2112	13	9445	3
Dy	4.27	2.45	5.20	1.72	3.99	2.09	3.34	0.00	3.31	0.00	3.14	0.84	3.41	2.30	4.06	2.08
Ho	0.88*	2.04	0.69*	1.57	0.65*	1.18	0.67*	1.67	0.71*	1.05	0.56*	1.48	0.58*	2.73	0.63*	0.85
Y	28.6	4.0	19.2	3.9	15.1	3.0	16.1	3.3	19.0	2.6	11.1	3.2	14.6	4.2	15.5	3.6
Er	2.86	0.74	1.08*	1.98	2.10	1.30	0.96*	1.66	1.67	1.64	0.80*	2.22	0.68*	4.65	2.49	1.13
Tm	0.52*	0.92	0.29*	1.47	0.20*	1.70	0.07*	3.10	0.30*	1.54	0.32*	0.83	0.32*	1.55	0.15*	1.88
Yb	3.87	1.23	2.38	1.01	1.11*	1.40	1.28	0.88	2.06	0.90	b.d.l.	-	0.65*	3.83	1.38*	2.05
Lu	0.45*	1.96	0.28*	2.66	0.19*	3.45	0.23*	3.07	b.d.l.	-	0.18*	2.81	b.d.l.	-	0.23*	3.22
V	127	23	161	16	214	16	200	13	191	14	156	17	98	34	179	16
Cr	b.d.l.	-	2309	55	3032	34	4049	29	3610	26	4856	25	3493	37	3270	31
Ni	134	12	209	8	254	6	297	4	267	6	298	5	260	8	369	5

b.d.l. - below detection limit

* - analyses with high uncertainty

Figure 1

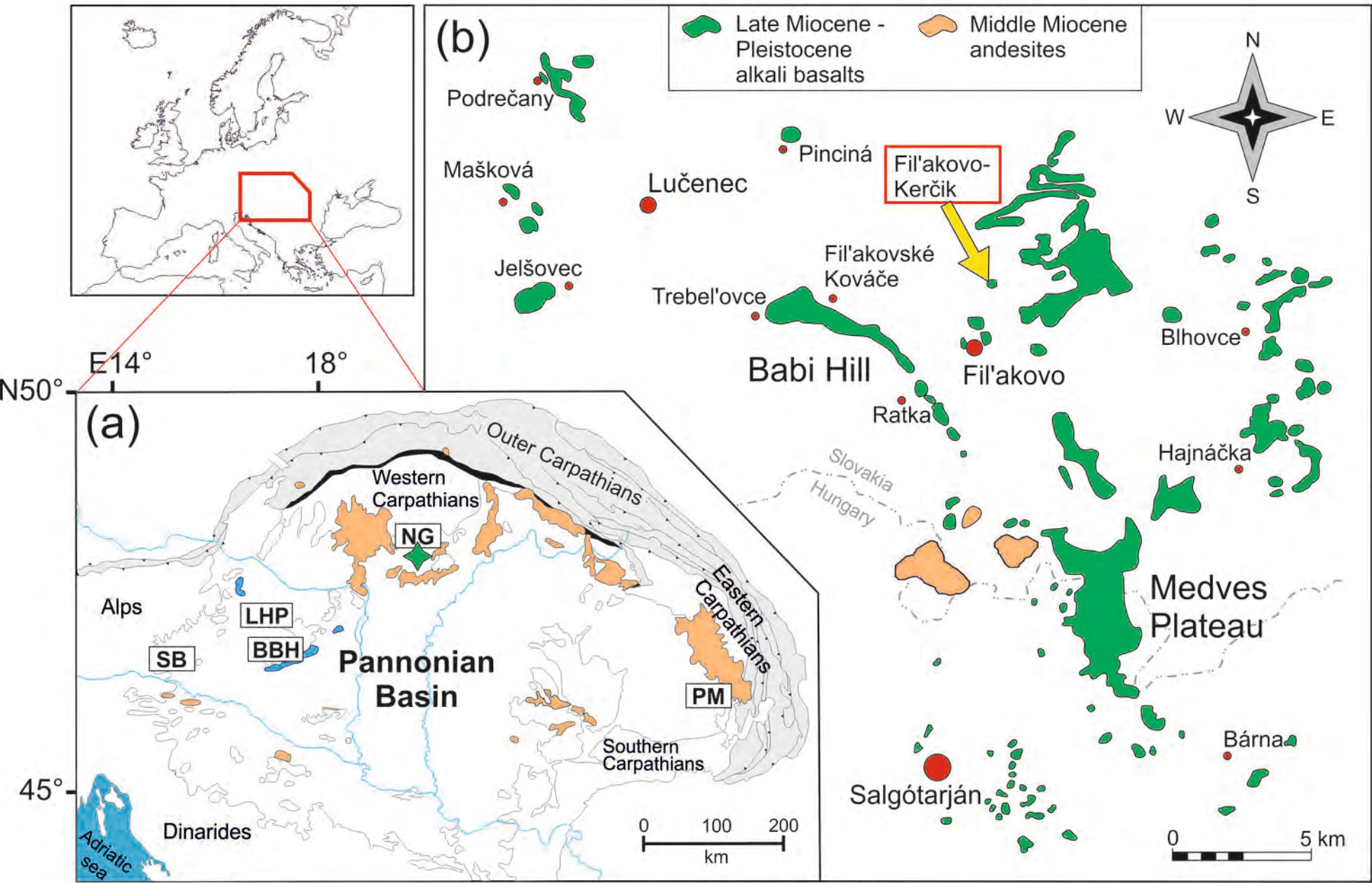
(b)
Late Miocene - Pleistocene alkali basalts
Middle Miocene andesites
N
W
E
S
Podrečany
Mašková
Jelšovec
Lučenec
Pinciná
Fil'akovo-Kerčik
Fil'akovské Kováče
Trebel'ovce
Babi Hill
Fil'akovo
Blhovce
Ratka
Hajnáčka
Slovakia
Hungary
Medves Plateau
Bárna
Salgótarján
0 5 km
E14°
18°
N50°
45°
(a)
Outer Carpathians
Western Carpathians
NG
Alps
LHP
SB
BBH
Pannonian Basin
Eastern Carpathians
PM
Southern Carpathians
Dinarides
Adriatic sea
0 100 200
km

Figure 2

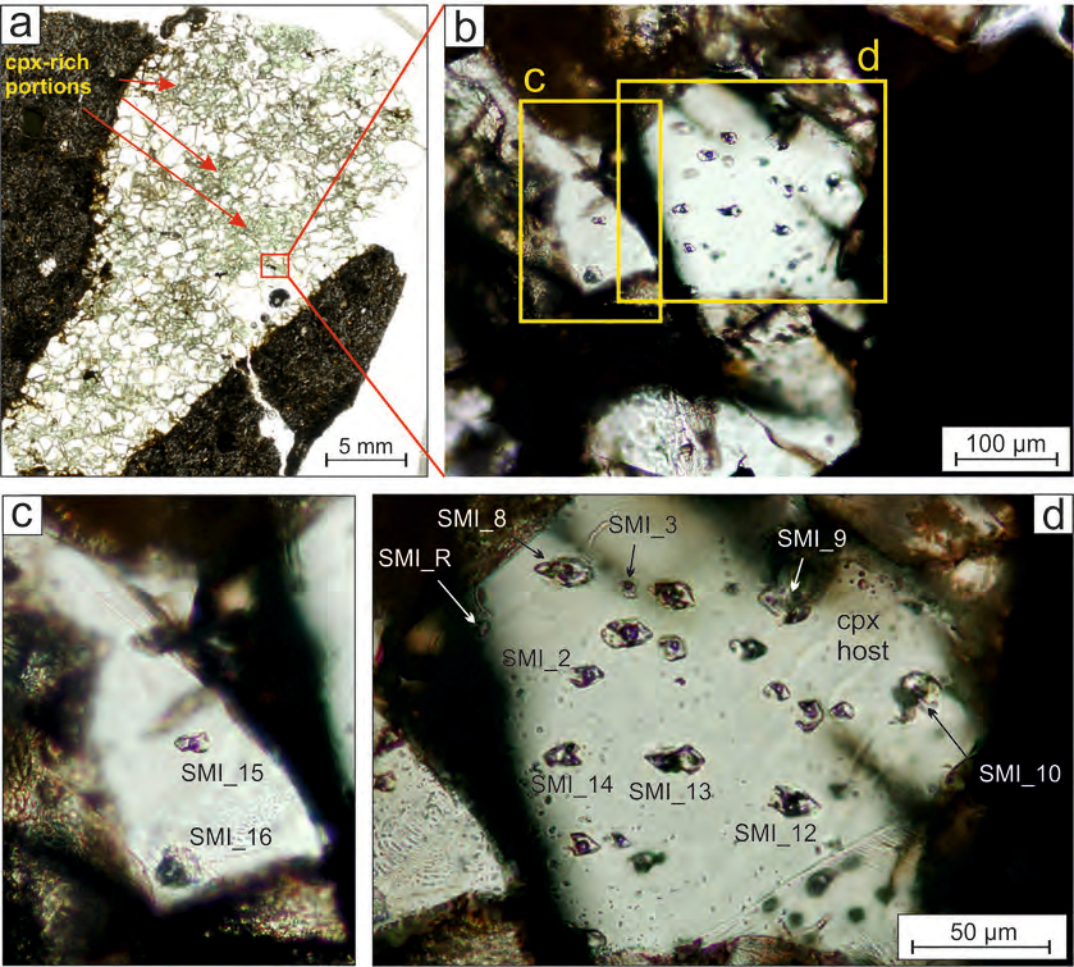
a
cpx-rich portions
5 mm
b
c
d
100 µm
c
SMI_15
SMI_16
d
SMI_8
SMI_3
SMI_9
SMI_R
cpx host
SMI_2
SMI_10
SMI_14
SMI_13
SMI_12
50 µm

Figure 3

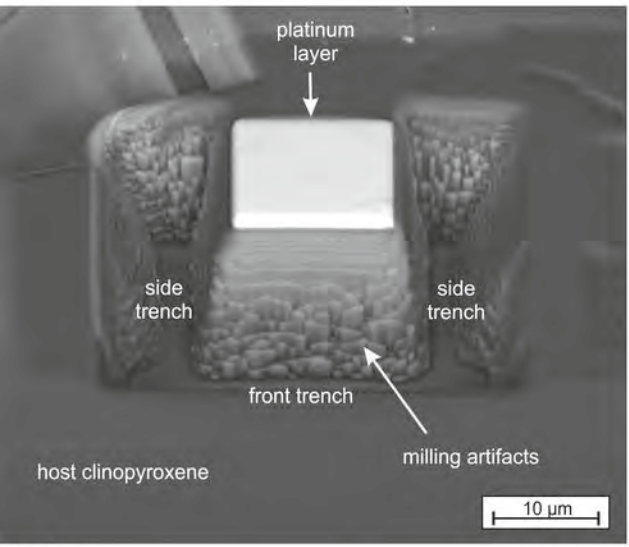
platinum layer
side trench
side trench
front trench
milling artifacts
host clinopyroxene
10 µm

(a)

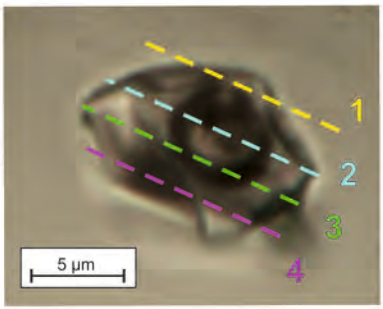
1
2
3
4
5 µm

(b)

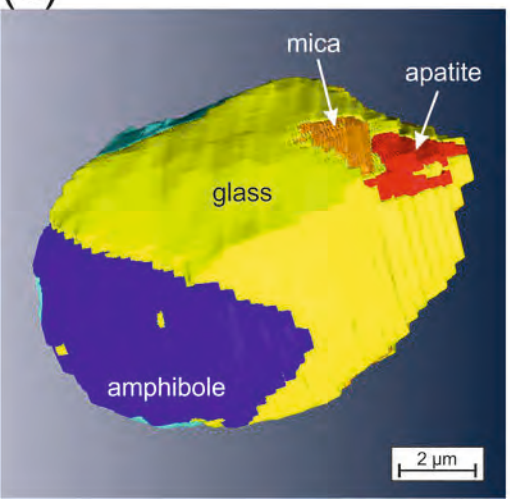
mica
apatite
glass
amphibole
2 µm

(c)

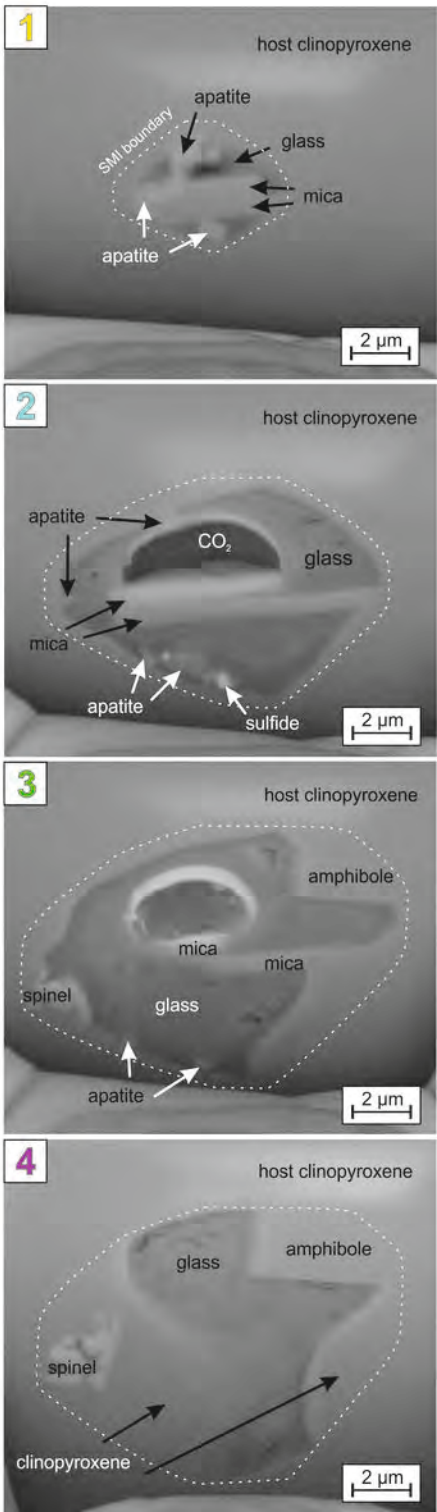
1
host clinopyroxene
apatite
SMI boundary
glass
mica
apatite
2 µm
2
host clinopyroxene
apatite
CO2
glass
mica
apatite
sulfide
2 µm
3
host clinopyroxene
amphibole
mica
mica
spinel
glass
apatite
2 µm
4
host clinopyroxene
glass
amphibole
spinel
clinopyroxene
2 µm

Figure 4

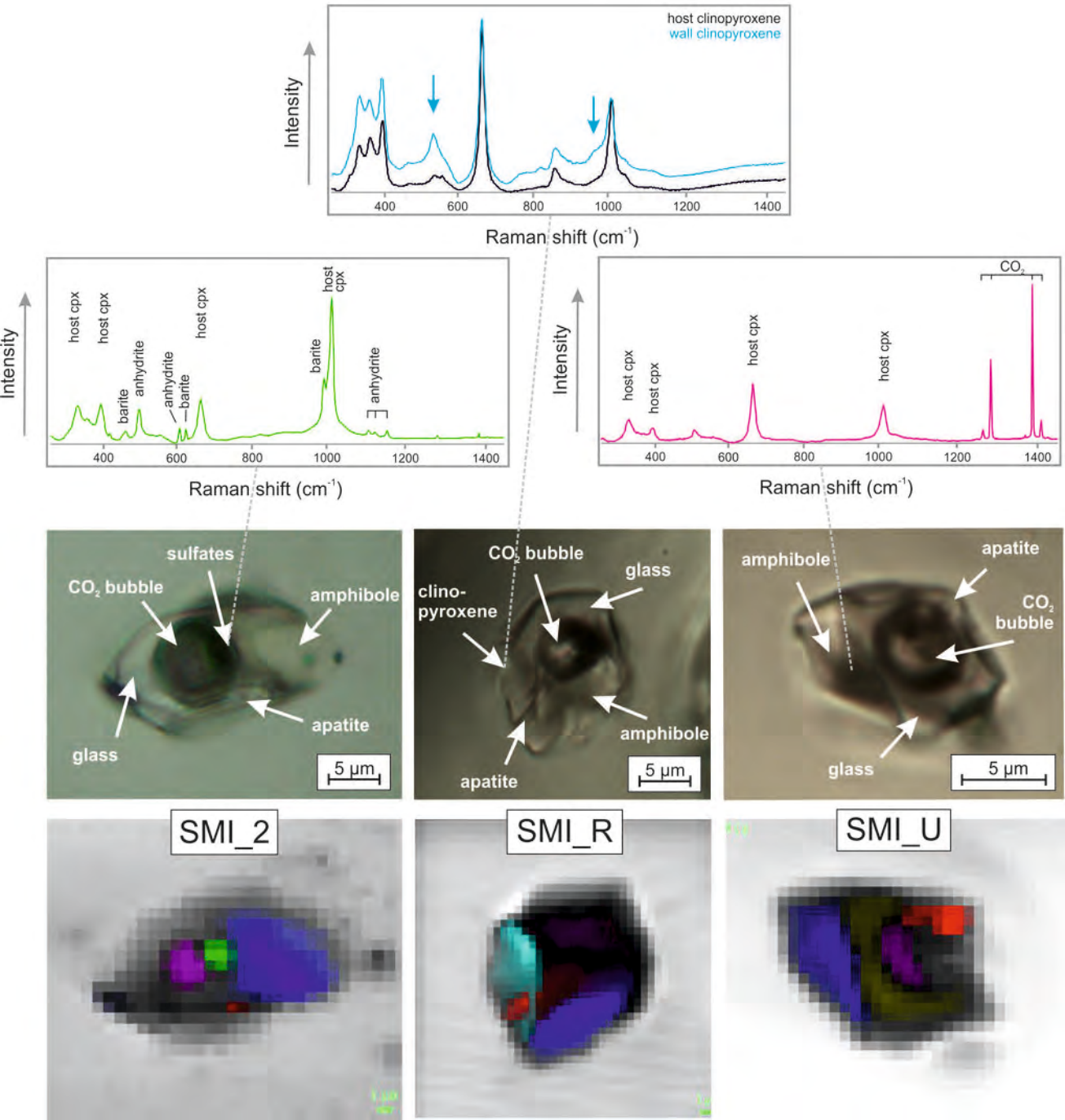
host clinopyroxene
wall clinopyroxene
Intensity
Raman shift (cm-1)
host cpx
barite
anhydrite
CO2
sulfates
CO2 bubble
amphibole
apatite
glass
clino-
pyroxene
5 μm
SMI_2
SMI_R
SMI_U

Figure 5

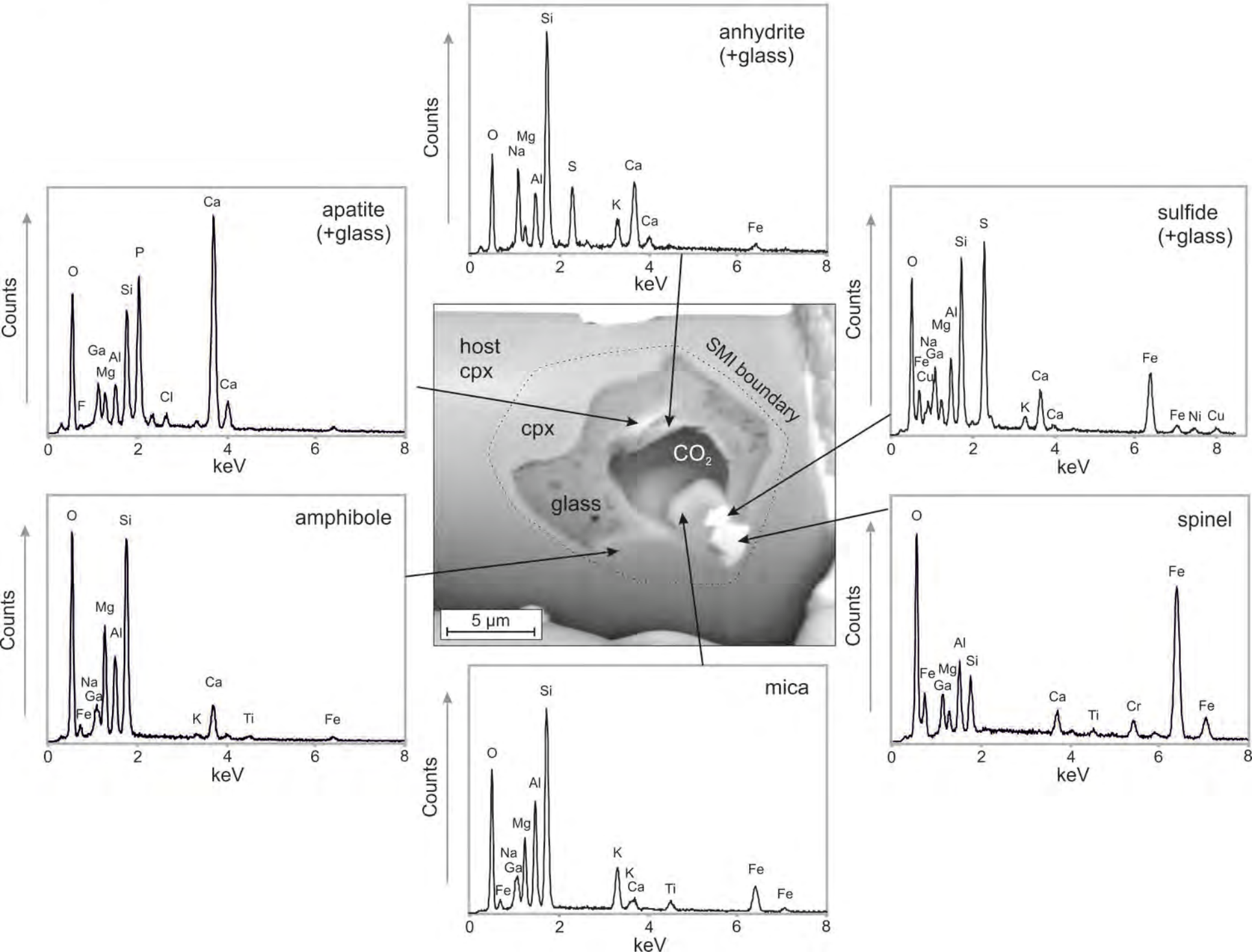
anhydrite
(+glass)
Counts
keV
O
Mg
Na
Al
Si
S
K
Ca
Ca
Fe
apatite
(+glass)
O
Si
P
Ca
Ga
Mg
Al
F
Cl
Ca
sulfide
(+glass)
O
Si
S
Al
Mg
Na
Ga
Fe
Cu
K
Ca
Ca
Fe
Fe Ni Cu
host
cpx
SMI boundary
cpx
CO2
glass
5 µm
amphibole
O
Si
Mg
Al
Na
Ga
Fe
K
Ca
Ti
Fe
spinel
O
Fe
Al
Si
Fe
Mg
Ga
Ca
Ti
Cr
Fe
mica
Si
O
Al
Mg
Na
Ga
Fe
K
K
Ca
Ti
Fe
Fe

Figure 6

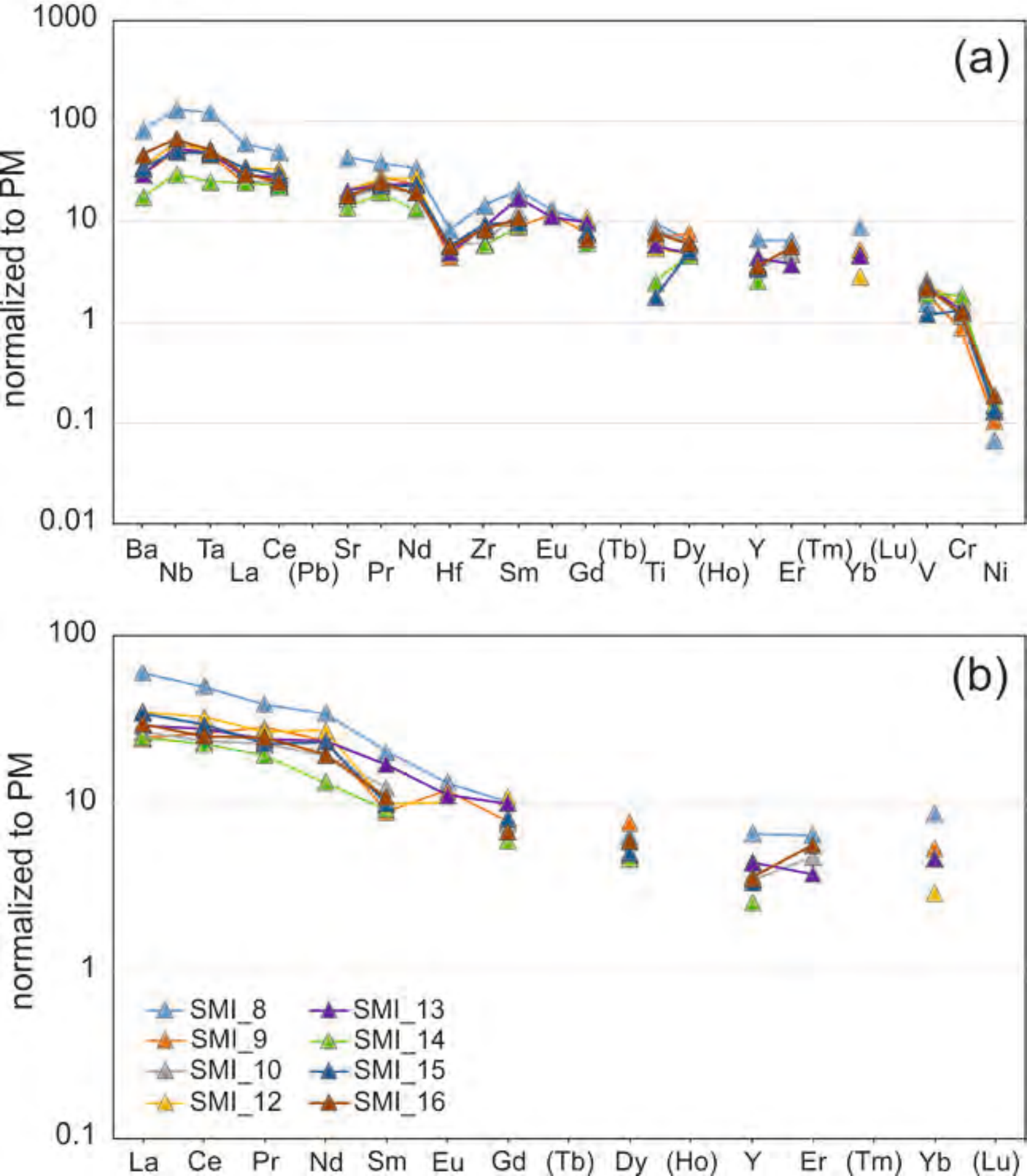
(a)
normalized to PM
1000
100
10
1
0.1
0.01
Ba
Nb
Ta
La
Ce
(Pb)
Sr
Pr
Nd
Hf
Zr
Sm
Eu
Gd
(Tb)
Ti
Dy
(Ho)
Y
Er
(Tm)
Yb
(Lu)
V
Cr
Ni
(b)
normalized to PM
100
10
1
0.1
SMI_8
SMI_9
SMI_10
SMI_12
SMI_13
SMI_14
SMI_15
SMI_16
La
Ce
Pr
Nd
Sm
Eu
Gd
(Tb)
Dy
(Ho)
Y
Er
(Tm)
Yb
(Lu)

Figure 7

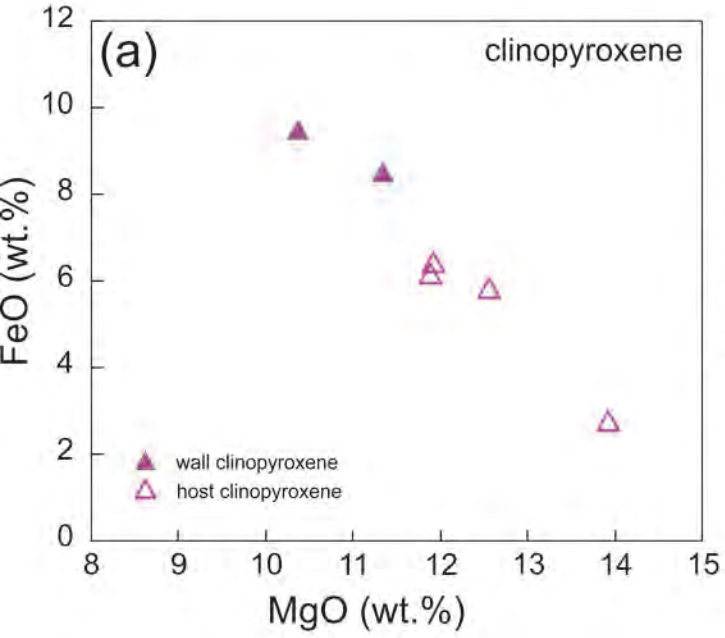
(a)
clinopyroxene
FeO (wt.%)
MgO (wt.%)
wall clinopyroxene
host clinopyroxene

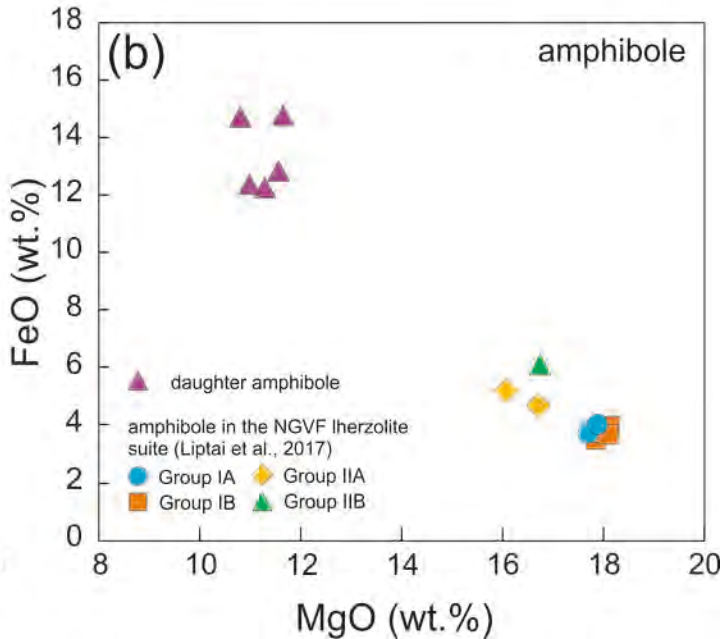
(b)
amphibole
FeO (wt.%)
MgO (wt.%)
daughter amphibole
amphibole in the NGVF lherzolite suite (Liptai et al., 2017)
Group IA
Group IB
Group IIA
Group IIB

Figure 8

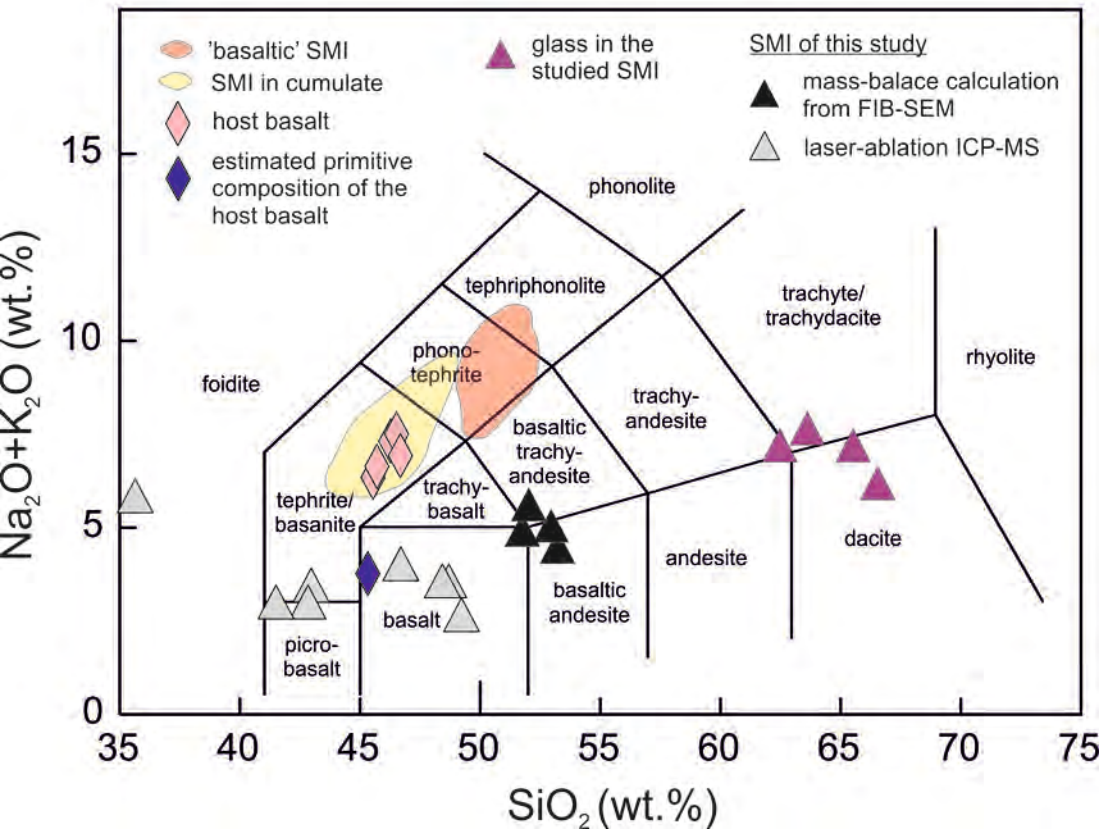
'basaltic' SMI
SMI in cumulate
host basalt
estimated primitive composition of the host basalt
glass in the studied SMI
SMI of this study
mass-balace calculation from FIB-SEM
laser-ablation ICP-MS
phonolite
tephriphonolite
trachyte/ trachydacite
rhyolite
foidite
phono-tephrite
trachy-andesite
basaltic trachy-andesite
tephrite/ basanite
trachy-basalt
dacite
andesite
basaltic andesite
basalt
picro-basalt
0
5
10
15
35
40
45
50
55
60
65
70
75
Na_2O+K_2O (wt.%)
SiO_2 (wt.%)

Figure 9

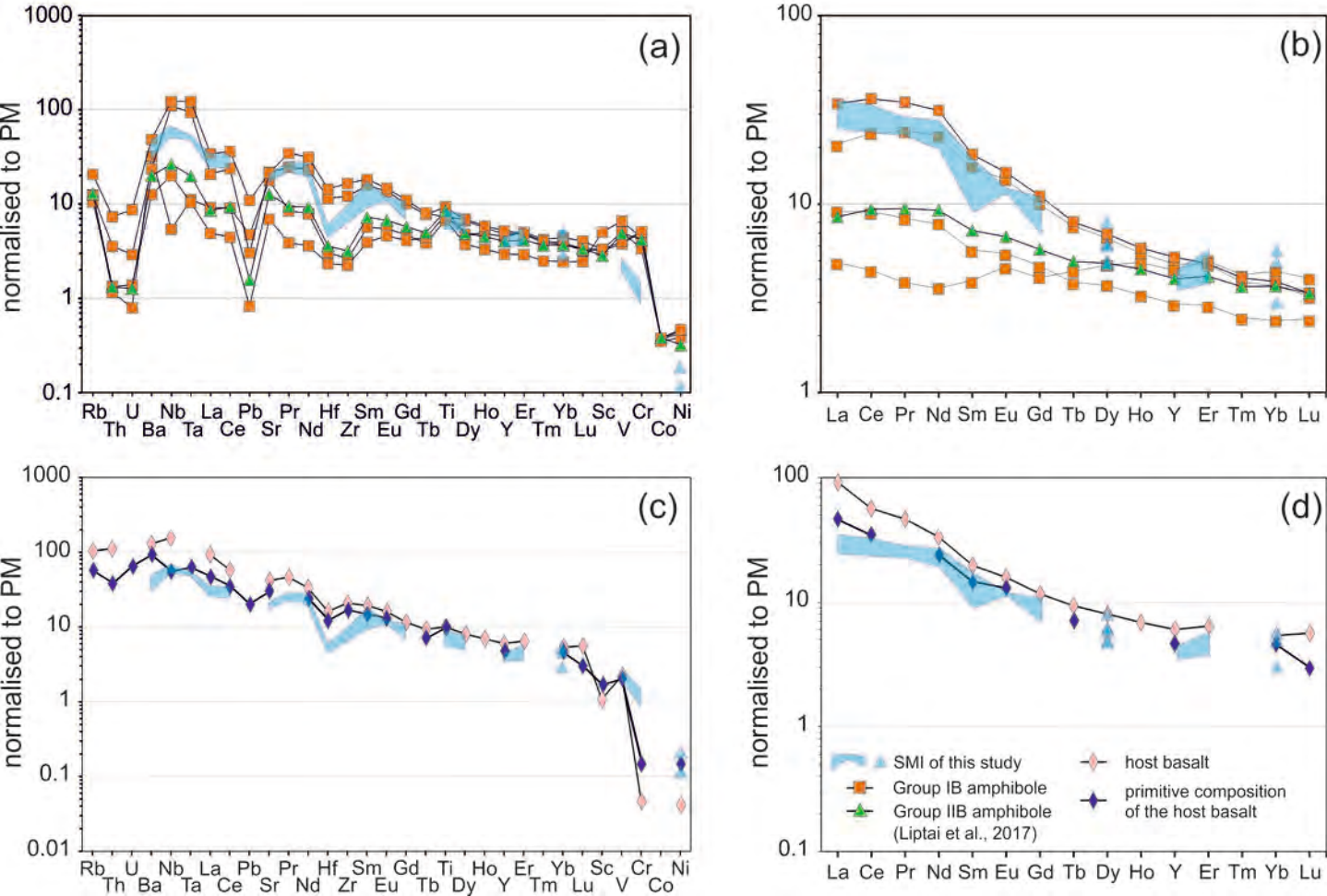
(a)
normalised to PM
1000
100
10
1
0.1
Rb U Nb La Pb Pr Hf Sm Gd Ti Ho Er Yb Sc Cr Ni
Th Ba Ta Ce Sr Nd Zr Eu Tb Dy Y Tm Lu V Co
(b)
normalised to PM
100
10
1
La Ce Pr Nd Sm Eu Gd Tb Dy Ho Y Er Tm Yb Lu
(c)
normalised to PM
1000
100
10
1
0.1
0.01
Rb U Nb La Pb Pr Hf Sm Gd Ti Ho Er Yb Sc Cr Ni
Th Ba Ta Ce Sr Nd Zr Eu Tb Dy Y Tm Lu V Co
(d)
normalised to PM
100
10
1
0.1
La Ce Pr Nd Sm Eu Gd Tb Dy Ho Y Er Tm Yb Lu
SMI of this study
Group IB amphibole
Group IIB amphibole
(Liptai et al., 2017)
host basalt
primitive composition
of the host basalt

Figure 10

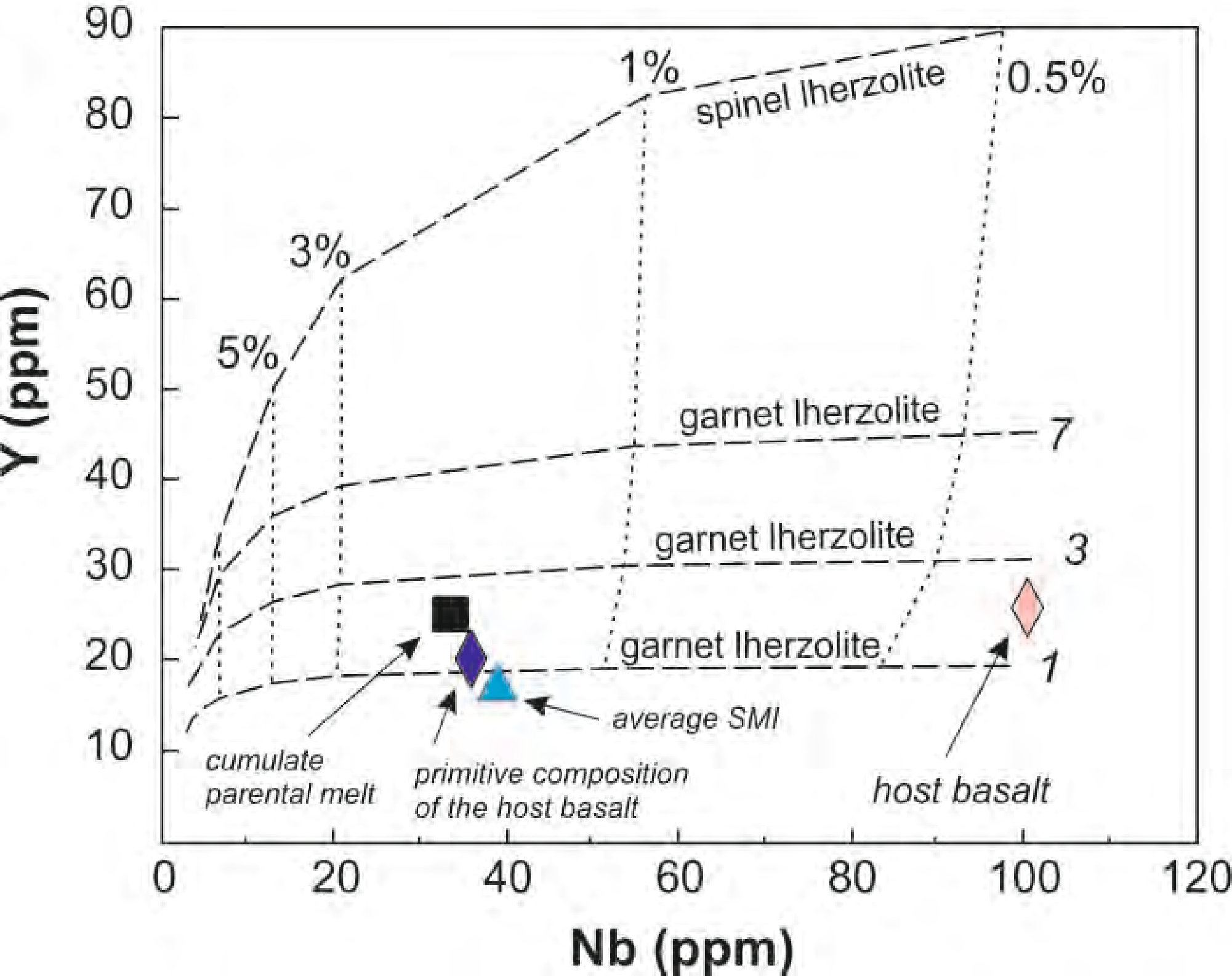
90
80
70
60
50
40
30
20
10
Y (ppm)
0
20
40
60
80
100
120
Nb (ppm)
1%
spinel lherzolite
0.5%
3%
5%
garnet lherzolite
7
garnet lherzolite
3
garnet lherzolite
1
average SMI
cumulate
parental melt
primitive composition
of the host basalt
host basalt

Figure 11

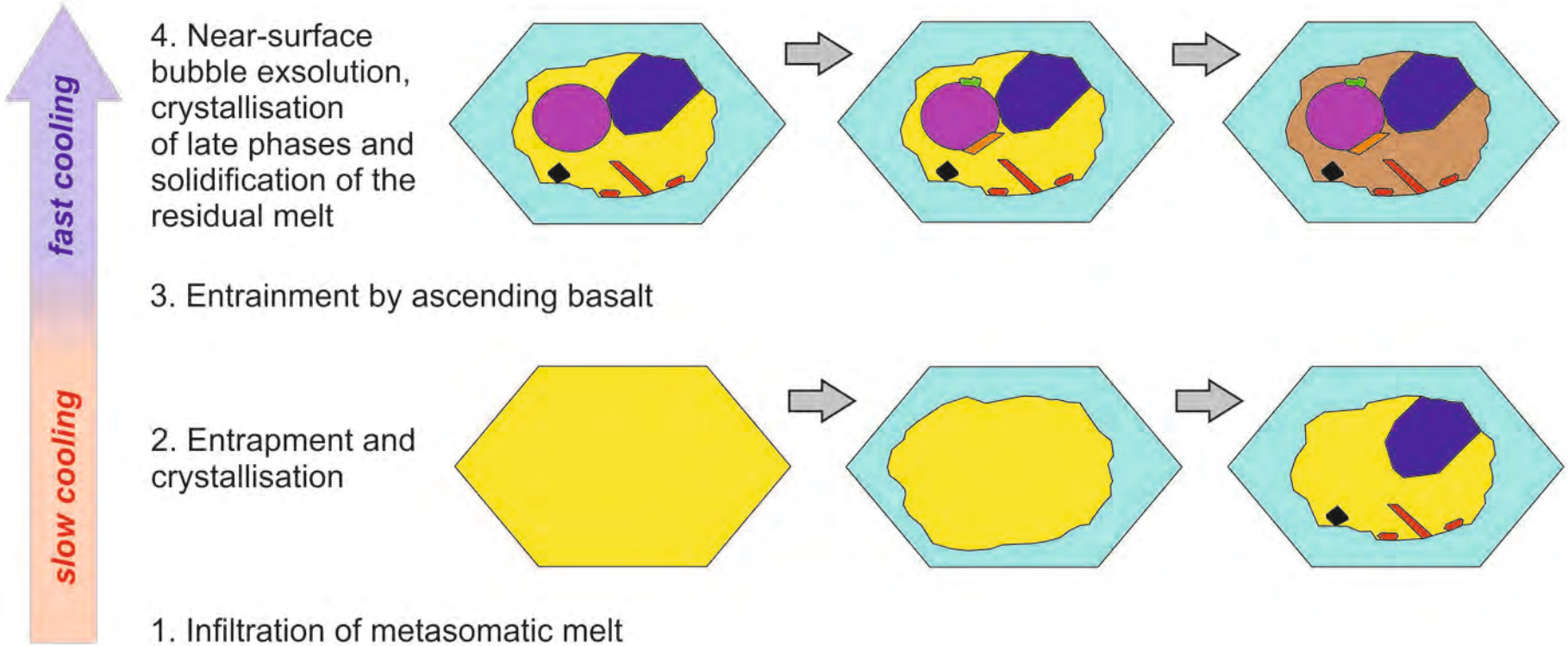
fast cooling
slow cooling
4. Near-surface bubble exsolution, crystallisation of late phases and solidification of the residual melt
3. Entrainment by ascending basalt
2. Entrapment and crystallisation
1. Infiltration of metasomatic melt